

# ALMA chemical survey of disk-outflow sources in Taurus (ALMA-DOT)

## VII: the layered molecular outflow from HL Tau and its relationship with the ringed disk

F. Bacciotti<sup>1</sup>, T. Nony<sup>1</sup>, L. Podio<sup>1</sup>, C. Dougados<sup>2</sup>, A. Garufi<sup>3,4</sup>, S. Cabrit<sup>2,5</sup>, C. Codella<sup>1</sup>, N. Zimniak<sup>2</sup>, and J. Ferreira<sup>2</sup>

<sup>1</sup> INAF - Osservatorio Astrofisico di Arcetri, Largo E. Fermi 5, 50125 Firenze, Italy  
e-mail: francesca.bacciotti@inaf.it

<sup>2</sup> Univ. Grenoble Alpes, CNRS, IPAG, 38000 Grenoble, France

<sup>3</sup> INAF – Istituto di Radioastronomia, Via P. Gobetti 101, 40129 Bologna, Italy

<sup>4</sup> Max-Planck-Institut für Astronomie, Königstuhl 17, 69117 Heidelberg, Germany

<sup>5</sup> PSL University, Sorbonne Université, Observatoire de Paris, LERMA, CNRS UMR 8112, 75014 Paris, France

Received -; accepted -

### ABSTRACT

**Context.** The ALMA image of the ringed disk around HL Tau stands out as the iconic signature of planet formation, but the origin of the observed substructures is still debated. The HL Tau system also drives a powerful bipolar wind, detected in atomic and molecular lines, that may have important feedback on the process.

**Aims.** The outermost component of the wind traced by CO emission is analyzed in detail to determine its relationship with the disk and its substructures.

**Methods.** A spectro-imaging investigation is conducted using ALMA observations of the <sup>12</sup>CO (2-1) line at 1.3 mm, with 0.2 km s<sup>-1</sup> and ~ 0".28 spectral and angular resolution, in the framework of the ALMA-DOT project. Relevant wind parameters are derived, allowing a tomographic reconstruction of the morphology and kinematics of the red-shifted lobe of the outflow, to compare with theoretical models.

**Results.** The data channel maps and position-velocity diagrams show a rich substructure of concatenated bubble- and arc-shaped features, whose size and distance from the source continuously increase with velocity. The superposition of such features generates the apparent conical shape. The spatio-kinematical properties suggest that the flow presents distinct nested shells with increasing velocity and faster acceleration going toward the axis, and rotating in the same sense of the disk. The wind parameters are compared with the predictions of magnetohydrodynamic (MHD) disk winds. Under this hypothesis, the launch radii of the three outermost shells are found to be at 55, 67 and 86 au from the star, coincident with regions of enhanced gas density in the disk. We derive a magnetic lever arm  $\lambda \sim 4 - 5$ , higher than that commonly adopted in models of MHD winds from the outer disk. Interpretations are discussed.

**Conclusions.** The properties of the CO outflow from HL Tau appear to be compatible with magnetized disk winds with launch radii in the region at 50 – 90 au from the source. As such, the wind may be capable of removing angular momentum also from the outer disk. The arrangement of the wind in nested shells with brighter emission rooted in rings of enhanced gas density could support the results of recent non-ideal MHD simulations according to which magnetic instabilities can spontaneously generate both the ring-gap system and a connected inhomogeneous layered wind, alternatively to the action of yet undetected protoplanets. Further observational analyses and comparisons with other classes of models will help establish the role of magnetic effects in the process of planet formation.

**Key words.** Protoplanetary disks – Jets and outflows – ISM: molecules – Stars: individual: HL Tau

### 1. Introduction

One of the most spectacular discoveries of the last decade has been the detection in the continuum emission at millimeter wavelengths of concentric gaps and rings in disks around young stars. The first example found is the disk around HL Tau. Observed with the Atacama Large Millimeter Array (ALMA)<sup>1</sup>, it showed in exquisite detail a sequence of concentric rings and gaps (ALMA Partnership et al. 2015), now commonly seen in many other disks (e.g. Andrews et al. 2018).

The first interpretation offered was that these gaps are carved by young massive planets embedded in the disk (e.g., Lodato et al. 2019). However, this scenario raises open issues, such as

the amount of mass necessary to produce massive planets at such large distances from the star (up to 100 au in HL Tau) and in such short timescales (less than 1 Myr). In addition, the predicted embedded planets inside the gaps remain elusive so far, except for PDS 70, where the "gap" actually is a large inner cavity (Keppler et al. 2018).

Several other disk processes are able to produce ring/gap structures. Perhaps the most generic are magnetic instabilities in the low-ionization "dead zone" (e.g., Suriano et al. 2018; Riols & Lesur 2019). This process could be widespread in young disks that harbor a residual primordial magnetic field. In this case, an inhomogeneous magnetohydrodynamic (MHD) disk wind (DW) is created, and the disk self-organizes in a system of rings and gaps, with denser wind layers launched from the rings and less

<sup>1</sup> <https://www.eso.org/sci/facilities/alma.html>

dense ones from the gaps (e.g. Suriano et al. 2019; Riols et al. 2020). An asymmetry also develops between the red and blue lobes (Béthune et al. 2017), as observed in almost all cases (e.g. Podio et al. 2011, 2021). Finding firm evidence for such layered MHD disk winds is thus an essential step in a clarification of the origin of disk substructures and of the role of magnetic fields in planet formation.

Signatures of layered outflows have indeed been found with ALMA in a growing number of young systems, in the form of rotating molecular winds flowing in a cavity of apparent conical shape (e.g. TMC1A, (Bjerkeli et al. 2016); HH 46/47, (Zhang et al. 2016, 2019); HH212 (Lee et al. 2017); DO Tau, (Fernández-López et al. 2020); HH 30, (Louvet et al. 2018; López-Vázquez et al. 2024; Ai et al. 2024); DG TauB (Zapata et al. 2015; de Valon et al. 2020, 2022); HH270mms1-A, (Omura et al. 2024); L1448-mm, (Nazari et al. 2024)). The CO outflow is associated in some cases with a coaxial molecular wind that emits in  $H_2$  lines, with a fast collimated atomic jet flowing along the axis of the system (e.g., HH 46/47, (Nisini et al. 2024), DG Tau B (Delabrosse et al. 2024)). The origin of the layered structure in these CO winds is debated. In addition to the magnetic instabilities mentioned above, other studies invoke the formation of swept-up wind shells (Zhang et al. 2019), peculiarities of the MHD disk-wind accretion/ejection engine (Louvet et al. 2018; de Valon et al. 2020), flow wiggling (de Valon et al. 2022), the action of the wings of subsequent bow shocks of time-variable jets, (Tabone et al. 2018; Rabenahary et al. 2022), or the evolution of a unified wind-angle magnetized flow with a jet-bearing X-wind (Shang et al. 2020, 2023; Ai et al. 2024).

Among these examples, HL Tau stands out as the first and only object where a possible coincidence between wind structure and the distribution of disk ring/gaps can be studied. In fact, in the other cases the flow is associated with a disk where no gaps and rings are detected. In some cases this can be due to the observing geometry (e.g. the edge-on disks of HH 30). In general, however, the accretion/ejection activity associated with young stellar objects is expected to decrease with the source evolutionary stage, hence powerful and bright molecular winds and jets are associated with Class 0 protostars (e.g., Lee et al. 2018; Tabone et al. 2017; Podio et al. 2021) while only faint molecular emission is associated with evolved Class II stars. On the other hand, substructures such as rings and gaps are commonly detected in pre-main sequence disks (e.g., SHARP LP, Andrews et al. 2018), while they are rarely detected in younger disks (see, e.g., Segura-Cox et al. 2020; Sheehan & Eisner 2017, 2018; de Valon et al. 2020). In this context, HL Tau is intermediate between an evolved accreting protostar (Class I) and a classical T Tauri star (Class II), and is associated with both a disk with clearly detected rings/gaps and a bright extended and structured outflow. This is therefore an ideal target for investigating the possible relation between the disk substructures and the wind properties and to test the proposed scenarios for their formation.

The central object, a young star of mass  $2.1 \pm 0.2 M_{\odot}$  (Yen et al. 2019a) is the source of a composite outflow seen at optical, infra-red, and mm wavelengths. The collimated atomic jet, that shines in shock-excited lines such as [S II] $\lambda\lambda 6716, 6731$ , H $\alpha$ , and [OI] $\lambda 6300$ , stretches out of the reflection nebula surrounding the star for about 1.5 along a direction PA  $\sim 50^\circ$  (Mundt et al. 1990; Anglada et al. 2007; Pyo et al. 2006; Movsessian et al. 2012). The system was imaged at  $0''.2$  resolution with Adaptive Optics in the near-infrared, showing a collimated jet in [FeII]  $1.64 \mu\text{m}$  and a surrounding wider angle warm wind emitting in  $H_2$   $2.12 \mu\text{m}$ , that flows in a conical cavity detected in scattered light (Takami et al. 2007; Beck et al. 2008). A coax-

ial molecular outflow has been observed in the CO(3–2) and CO(1–0) lines (Lumbreras & Zapata 2014; ALMA Partnership et al. 2015; Klaassen et al. 2016). The data show a prominent conical redshifted flow to the south-west of HL Tau, with the axis almost aligned with the atomic jet and a full opening angle of about  $60^\circ$ . The north-eastern lobe is much fainter and appears as a wide cavity dispersed within the ambient.

In this paper we investigate the structure of the CO outflow in more detail analyzing a dataset obtained within the program ALMA-DOT (ALMA chemical survey of Disk-Outflow sources in Taurus), an observational campaign aimed at characterizing the gas in disks and outflows of embedded sources in the Taurus star-forming region. The high angular/spectral resolution of ALMA allow us to disentangle and characterize the emission from the various elements of the system (disk, outflows, streamers, envelope). Previous papers in the ALMA-DOT series focus on the chemical properties of the disks (Podio et al. 2019, 2020a,b; Codella et al. 2020) and of the associated streamers and outflows (Garufi et al. 2020, 2022), while Garufi et al. (2021) describes the collective properties of the examined targets as a whole. The present work focuses on the observations of the molecular outflow around HL Tau, as imaged in the line of  $^{12}\text{CO}$  (2–1) at 1.3 mm with a resolution of  $0''.28$ , and on the implications of these findings for the structure of the disk.

The paper is organized as follows. Section 2 details the observations and the reduction of the data. Section 3 describes the results obtained, while the derived hypothesis for the structure of the wind is described in Section 4. In Section 5 we discuss the comparison of the results with theoretical models in an MHD disk wind scenario. The conclusions of this study and the perspectives for future analyses are outlined in Section 6.

## 2. Observations and data reduction

Cycle 6 observations of the ALMA-DOT campaign (Podio et al. 2019) were taken with ALMA-Band 6 on October 28, 2018 in an extended configuration with baselines ranging from 15 m to 1.4 km (project 2018.1.01037.S, PI: L. Podio). The field of view is a circular region around HL Tau of radius  $\sim 18''.5$ , corresponding to about  $2.7 \cdot 10^3$  au at the distance of the source, 147.3 pc (Galli et al. 2018). The integration time sums up to  $\sim 110$  minutes (Garufi et al. 2021). The bandpass and phase calibrators were J0423-0120 and J0510+1800, respectively. The correlator setup consisted of high resolution (0.141 MHz) spectral windows (SPWs) covering  $^{12}\text{CO}$  (2–1), CN (2–1), o- $\text{H}_2\text{CO}$  ( $3_{1,2}-2_{1,1}$ ) CS (5–4), and  $\text{CH}_3\text{OH}$  ( $5_{0,5}-4_{0,4}$ ) (A). The molecular parameters were taken from the Cologne Database of Molecular Spectroscopy (CDMS) (Müller et al. 2001). In this paper, we focus on the  $^{12}\text{CO}$  (2–1) emission (rest frequency 230.538 GHz), while the description in other molecular lines can be found in Garufi et al. (2020).

Data were reduced using the standard procedure using the Common Astronomy Software Applications package (CASA, McMullin et al. 2007) version 4.7.2. Self-calibration was performed on the continuum emission and applied on the line-free continuum, and the continuum subtracted line emission. The procedure improved the continuum S/N by a factor of 3.3. The final continuum maps and spectral cubes were produced with `tclean` by applying a manually selected mask to the signal and iterating until the residuals revealed no significant source emission. We adopted Briggs weighting with `robust=0.0` for the bright CO line, to maximize angular resolution, and set a channel width of  $0.2 \text{ km s}^{-1}$ . The clean beam of the self-calibrated maps in CO is  $0.26'' \times 0.31''$  with a PA of  $-3.12^\circ$ . The r.m.s. noise per

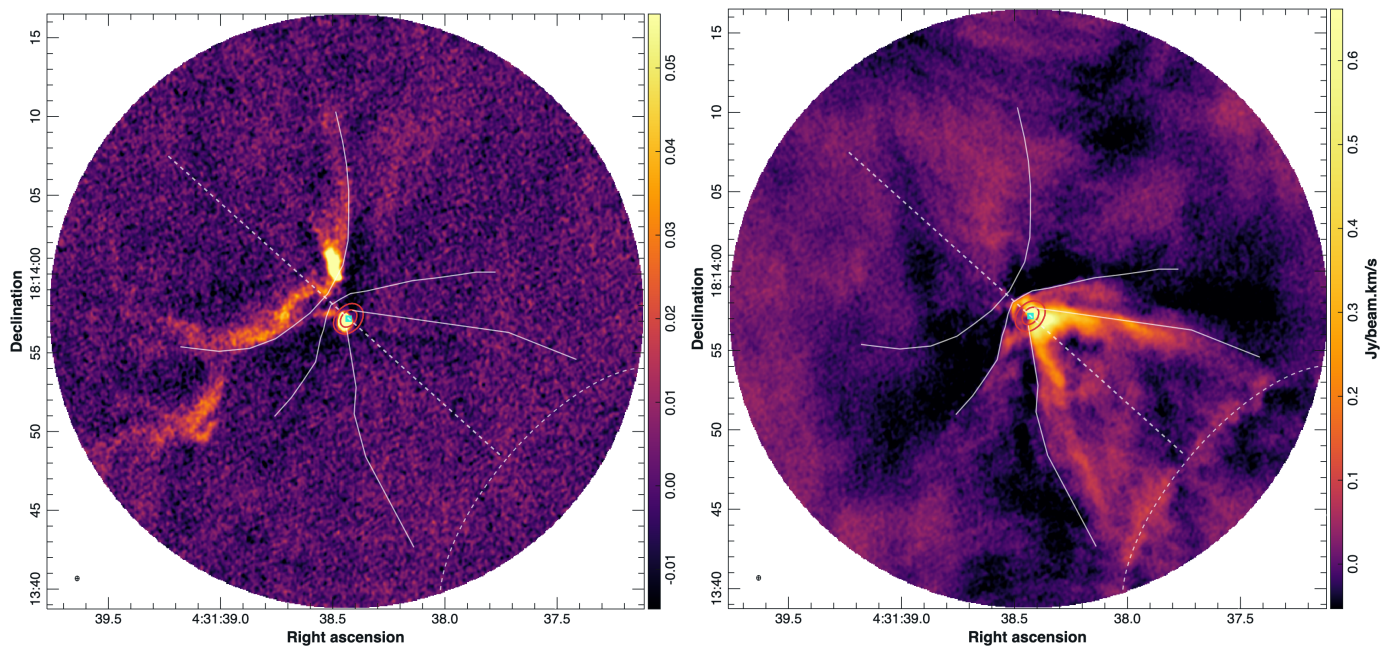


**Fig. 1.** *Left:* Moment 0 maps of the CO (2–1) emission integrated over the velocity interval  $V_{\text{LSR}} = (-10, +3) \text{ km s}^{-1}$ , highlighting the morphology of the blue-shifted outflow lobe. The red contours at the center of the panel corresponds to the disk continuum emission at 1.3 mm drawn at  $[10, 200]\sigma_c$ , with  $\sigma_c = 1.2 \cdot 10^{-4} \text{ Jy beam}^{-1}$ . The white line at  $\text{PA}=48^\circ$  indicates the orientation of the disk minor axis, and the white solid curves outline the spatial limits of the main wind components described in the text. *Right:* same as left panel, but with velocity integration range  $V_{\text{LSR}} = (+8, +30) \text{ km s}^{-1}$ , illustrating the structure of the red-shifted lobe. The beam is drawn in the bottom left corner. Note the difference in brightness between the two lobes, with the blue-shifted one being about ten times fainter.

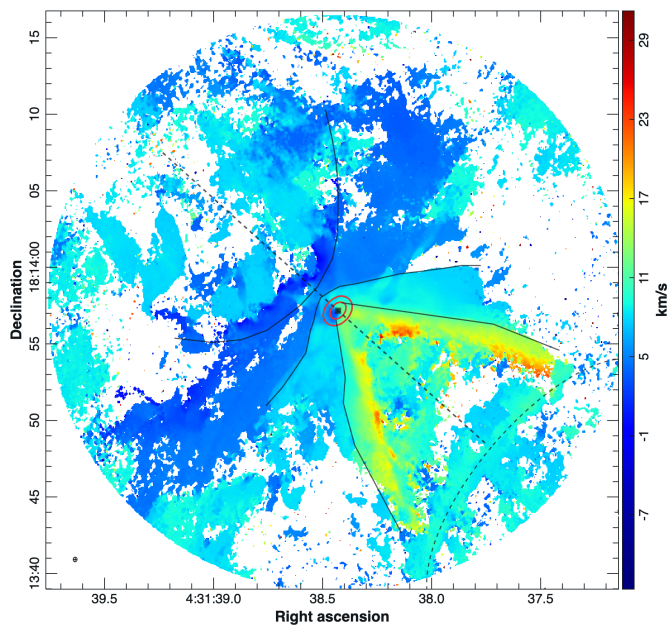


**Fig. 2.** Moment 1 map of the CO (2–1) emission over the velocity interval  $V_{\text{LSR}} = (-10, +32) \text{ km s}^{-1}$ . Black solid curves and disk contours are as in Fig. 1. The map was produced using a  $4\sigma$  clipping.

channel is  $\sigma_{\text{CO}} = 2 \text{ mJy beam}^{-1}$ . The beam in the continuum images is  $0.23'' \times 0.26''$  with  $\text{PA} = -6.77^\circ$ . The r.m.s. for the continuum image is  $\sigma_c = 1.2 \cdot 10^{-4} \text{ Jy beam}^{-1}$ .

### 3. Results

#### 3.1. Continuum emission

The continuum at 1.3 mm has an integrated flux of  $844.9 \pm 1.9 \text{ mJy}$ , with peak intensity of  $95.48 \pm 0.19 \text{ mJy beam}^{-1}$  located at R.A.  $04^{\text{h}} 31^{\text{m}} 38^{\text{s}}.43$ , and Dec.  $18^\circ 13' 57''.17$ . At our angular resolution the intensity distribution is smooth, and the sequence of rings and gaps is not visible. The FWHM along the major and minor axes, determined with a 2D Gaussian fit deconvolved from the beam, is  $0''.81$  and  $0''.56$ , respectively. From these values, we estimate an inclination angle  $i$  of the disk with respect to the line of sight of  $\sim 46^\circ.5$ . The fit gives a disk position angle,  $\text{PA}_{\text{disk}} = +138^\circ.06 \pm 0^\circ.87$ . Both values agree with those reported in ALMA Partnership et al. (2015),  $i = 46^\circ.72 \pm 0^\circ.05$ ,  $\text{PA}_{\text{disk}} = +138^\circ.02 \pm 0^\circ.07$ .

#### 3.2. CO (2–1) emission

The ALMA datacube in the CO (2–1) line consists of 290 velocity channels with  $V_{\text{LSR}}$  ranging from  $-26$  to  $31.8 \text{ km s}^{-1}$ , in steps of  $0.2 \text{ km s}^{-1}$ . The emission from the outflow is detected from  $-10 \text{ km s}^{-1}$  to  $+32 \text{ km s}^{-1}$ . The systemic velocity is  $V_{\text{sys}} = +7.1 \text{ km s}^{-1}$  (Garufi et al. 2021).

Figure 1 presents the intensity integrated over velocity (moment-0 map) in the full field of view. The left panel shows the emission integrated over the blue-shifted velocity range  $V_{\text{LSR}} = (-10, +3)$ , while the integration in the right panel is for  $V_{\text{LSR}}$  velocities between  $+8$  and  $+30 \text{ km s}^{-1}$ , illustrating the red-shifted emission. The faint blue-shifted emission is distributed along a wide-angle cavity of semi-spherical shape pointing towards the north-east (NE), with a distinct bright feature on the northern side. The emission in the red-shifted south-west (SW) lobe presents two main components, an inner flow of apparent conical shape with full opening angle of about  $60^\circ$  around an

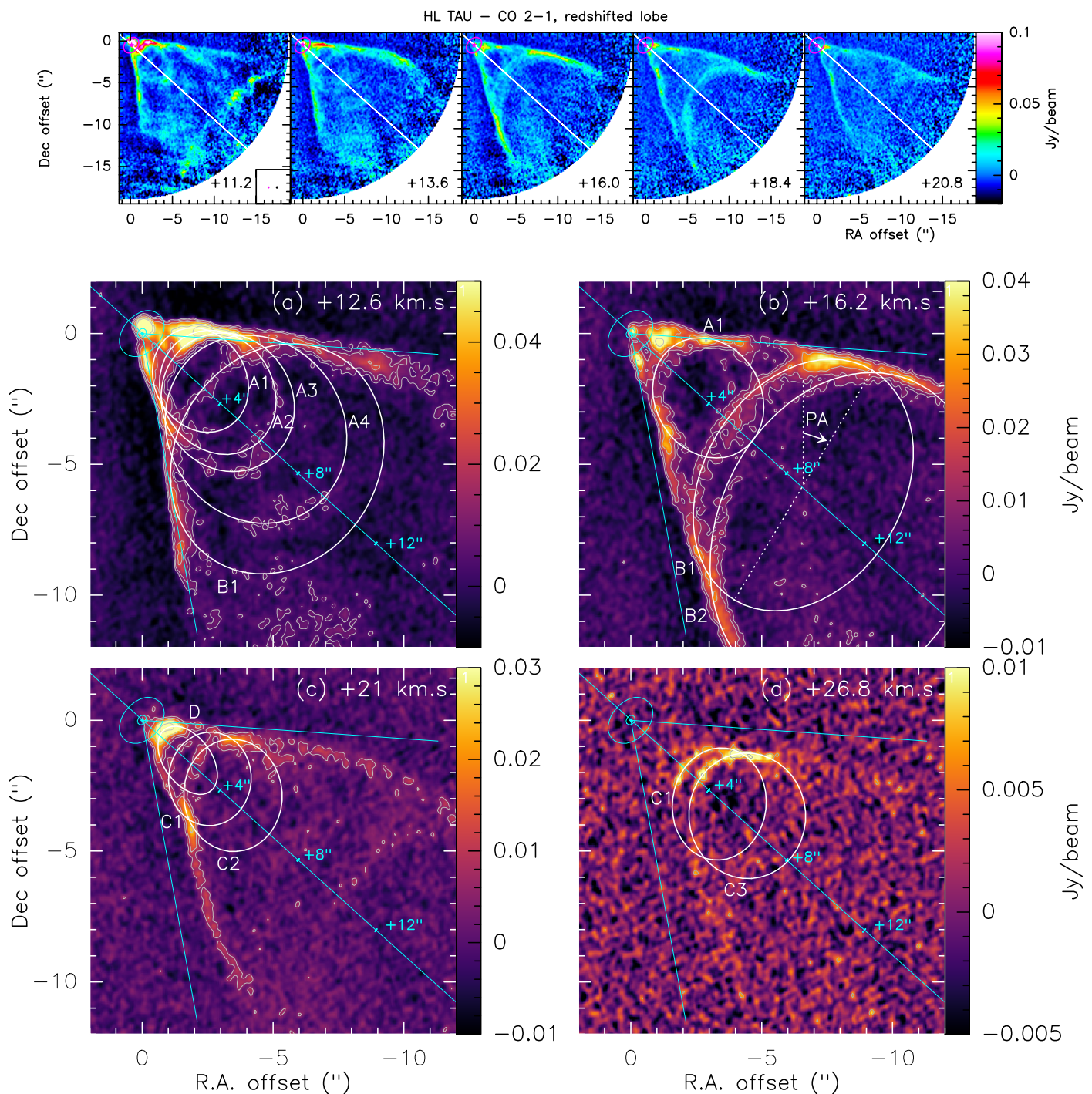


**Fig. 3.** *Top panel:* Channel maps at selected  $V_{\text{LSR}}$  velocities of the red-shifted emission in the CO (2-1) line in the SW outflow lobe. The star symbol and the magenta contour indicate the position of the source and the disk emission at  $1.3\text{ mm}$  drawn at  $10\sigma_c$ , respectively. The white solid line lies at  $\text{PA}=228^\circ$ . The magenta and black dots in the lower right corner of the leftmost panel report the beam size in the continuum and line observations, respectively. *Center and bottom panels:* Zoom on channel maps at selected  $V_{\text{LSR}}$  velocities, illustrating the system of arcs and bubble-like substructures visible in the red-shifted outflow. The CO emission contours are drawn at  $[3, 6, 12, 24, 48]\sigma_{\text{CO}}$ . Two cyan contours of the  $1.3\text{ mm}$  continuum at  $[30, 700]\sigma_c$  indicate the disk position, with the direction of its minor axis highlighted by the cyan line at  $\text{PA}=228^\circ$ . Two other cyan lines mark the  $\pm 38^\circ$  average opening angle of the apparent conical cavity at  $12.6\text{ km s}^{-1}$ , to illustrate the narrowing of the flow with increasing velocity. In the vicinity of the source, a number of arcs are seen to combine to form closed curves. Farther from the source only arcs open toward SW are visible. The superposed white ellipses are examples of visual fits to the identified features, labelled in families shearing common properties. The orientation of the features deviates slightly from  $\text{PA}=228^\circ$ , as illustrated in panel *b* for ellipse B1, whose major axis is oriented at  $\text{PA} = 329^\circ$ .

axis oriented at  $\text{PA} = 228^\circ$  (coinciding with the minor axis of the disk) and an outer faint wide wind of aperture  $\sim 120^\circ$  that surrounds in projection both the disk and the base of the inner outflow. The spatial limits of these components are indicated by

solid white lines. A ridge of molecular emission is evident at 14" from the source. This is part of a wider elliptical feature, as shown in ALMA Partnership et al. (2015), Fig. 1, and reported here with a dashed white elliptical curve.

The velocity-weighted intensity (moment-1 map) of the emission is presented in Fig. 2. The NE sector hosts uncollimated blue-shifted material, while the red-shifted SW lobe is structured. The transition in velocity between the two wind components identified in the moment-0 map shows the outer wide wind being slower than  $10 \text{ km s}^{-1}$ , while the inner flow has increasing velocities from the border toward the axis, up to about  $30 \text{ km s}^{-1}$ .

The asymmetry in the two outflow lobes may be partly due to HL Tau being located on the wall of a large-scale molecular bubble inflated by the nearby XZ Tau, at 23" east of the source (Welch et al. 2000; Yen et al. 2019b). The expanding bubble may have compressed the outer envelope of HL Tau on its NE side, smashing the CO cavity, while the SW lobe remained unaffected. Signatures of such a large-scale bubble are visible at low blue-shifted velocities in Fig. 2.

The squared  $10''$  at the center of the region were discussed in Garufi et al. (2022), where the kinematics of the rotating disk is analyzed from the same dataset, as well as possible accretion streamers.

### 3.3. Velocity channel maps

A comprehensive atlas of the channel maps of the CO (2-1) emission is given in Appendix A. The analysis of the individual channels reveals a faint but very rich flow substructure, not visible in moment-0 and moment-1 maps. Emission in the blue lobe is barely detectable, but the signal is strong in the red-shifted lobe, allowing a detailed inspection. In the following, we concentrate the analysis on this part of the outflow, deferring the study of the properties of the other component to the next paper in the ALMA-DOT series.

A selection of channel maps illustrating the configuration of the inner flow in the red-shifted SW lobe is presented in the top panel of Fig. 3. The maps show an apparent conical structure, with half-opening angle decreasing with velocity, from about  $40^\circ$  at  $10 \text{ km s}^{-1}$  to  $27^\circ$  at  $26 \text{ km s}^{-1}$ .

Inscribed in the conical apparent shape, one finds a series of ‘bubbles’ and ‘arcs’ of different size, position and brightness. The arcs appear to be part of concatenated closed curves that can be visually fitted by ellipses, as illustrated in Fig. 3. About ten such structures can be identified, grouped in four families that we label as A, B, C, D. Each feature continuously changes size and position with channel maps and acquires progressively larger extension and separation from the star as the  $V_{\text{LSR}}$  velocity increases, but maintains its shape unaltered. Arcs ‘A’ are observed at low velocity ( $10\text{-}16 \text{ km s}^{-1}$ , see Fig. 3a-b) and at small separation. Despite the blending of the emission on the source side and the fragmented appearance at larger distances, these structures clearly form closed bubble-like curves expanding with increasing velocities. Arcs B1 and B2 have a large extension and only show the convex branch on the side of the source. They can be followed over a wide range of velocities, from  $11$  to  $19 \text{ km s}^{-1}$ , in which they continuously change position from  $3''$  to  $10''$  from the source, as illustrated in Fig. A.3. Arcs C are visible only at high velocity ( $20\text{-}29 \text{ km s}^{-1}$ , see Fig. 3c-d). They are relatively faint, but their positional shift with velocity can be clearly recognized. Finally, the bright arc D is visible at a small distance from the source (about  $0''.9$ ) and at intermediate velocities ( $20 \text{ km s}^{-1}$ , see Fig. 3c). The orientation of the features deviates slightly from

that of the axis of the system. This is illustrated, for example, in panel *b* of Fig. 3.

In general, inspection of channel maps makes clear that the flow cannot be defined to have a simple and continuous conical shape. In contrast, the apparent conical border is revealed to arise from the superposition of the discrete limb-brightened arc-shaped substructures.

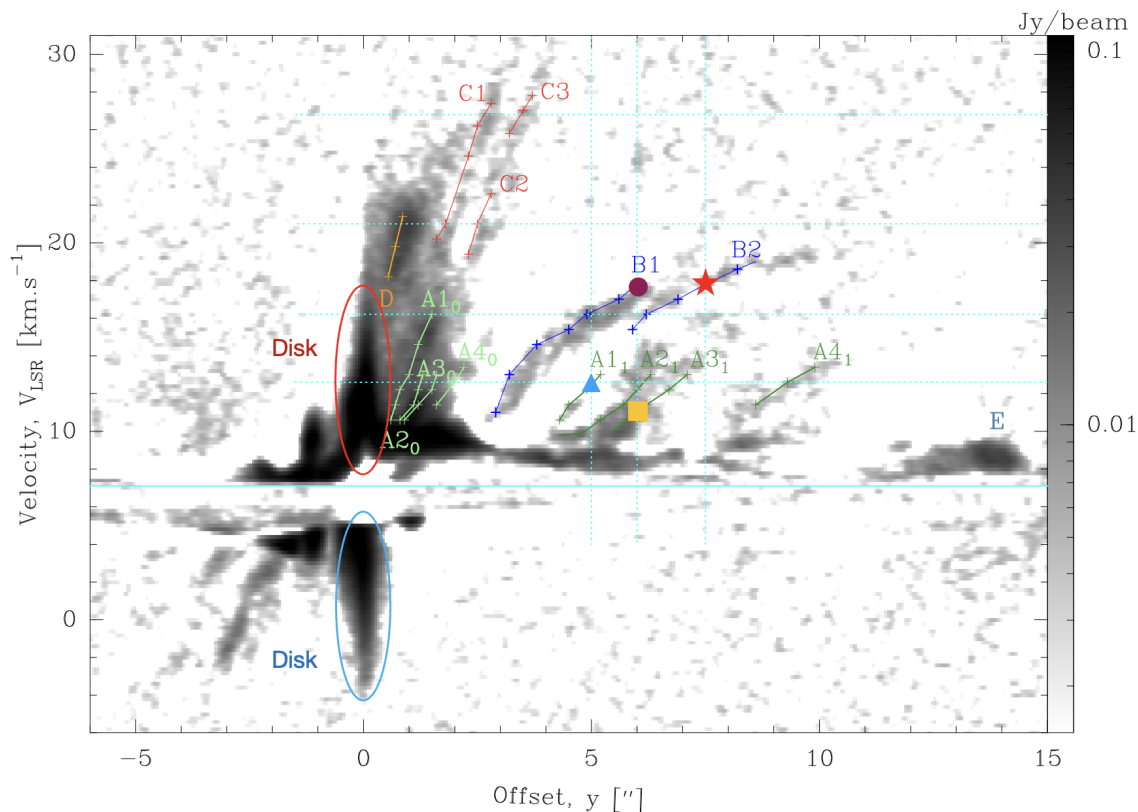
### 3.4. Parallel Position-Velocity diagram

Figure 4 illustrates the Position-Velocity diagram obtained with a virtual slit  $0''.3$  wide (comparable with the beam size) positioned along the axis ( $\text{PA}=228^\circ$ ). The diagram (hereafter referred to as  $\text{PV}_{\parallel}$ ) collects emission from both circumstellar material and extended wind. The emission within offset  $y = \pm 2$  arcseconds from the source is due partly to the disk and partly from the base of the wind, whose large opening produces contributions in both red-shifted and blue-shifted velocities on each side (e.g., Klaassen et al. 2016). The emission at larger offsets and velocities comes only from the extended wind.

The striking characteristic of the diagram is the fact that the emission in the wind region is not continuous, but it is distributed in a fan of separated traces on both sides of the source (superposed to a low intensity more homogeneous emission in the region  $y < 2''$  and  $V_{\text{rad}} < 23 \text{ km s}^{-1}$ ). In the blue lobe, at least three linear traces are seen to propagate towards larger blue-shifted  $V_{\text{LSR}}$  velocity. On the SW red-shifted side, more than ten traces can be recognized. Within the first  $4''$  a fan of almost linear traces opens from the source reaching high velocities, up to at least  $V_{\text{LSR}} \sim 28 \text{ km s}^{-1}$ . For each of them, the velocity appears to increase linearly with offset, in a way reminiscent of a ‘Hubble law’ trend. This group of traces displays the steepest slope, that is, the highest apparent acceleration, among the features in the diagram. A second fainter fan of almost linear segments is observed between  $4$  and  $11''$ , with lower  $V_{\text{LSR}}$  velocities up to  $\sim 15 \text{ km s}^{-1}$ . Interposed between the two groups one finds two extended traces of parabolic-like shape, reaching velocities as high as  $20 \text{ km s}^{-1}$ .

The substructures detected in the diagram are suggestive of a common origin with the arc- and bubble-shaped features identified in the channel maps. To test this hypothesis, for each of the ellipses described in Section 3.3, and for each velocity channel, we report on the red-shifted portion of the  $\text{PV}_{\parallel}$  diagram the  $y$  offset of the intersections of the fitted ellipses with the flow axis (cyan line in Fig. 3). Subscripts ‘0’ and ‘1’ indicate the intersections of the side of the ellipse closer and farther from the source, respectively. The broken lines obtained by connecting the points relative to the same side of each ellipse are strikingly coincident with sections of the emission branches in the diagram.

The first group of filaments reaching high velocities corresponds to arcs D (orange), C (red) and to the intersections of type ‘0’ of features A (green). The second group corresponds to the SW sides of the A ellipses, marked as ‘1’ (green). Given the inclination angle of the wind in space ( $i=46^\circ.5$ ), the  $A_0$  traces appear to correspond to the rear side of the flow and the  $A_1$  traces to the front side. Note that the  $A_0$  and  $A_1$  traces appear in the same order from the source, in a way coherent with the fact that in the channel maps the ellipses of the A family are concatenated rather than nested. The long parabolic traces correspond to the features of the B family (in blue). These filaments well reproduce the consistent shift in position with velocity described in Fig. A.3. The emission peak at offset  $y = 14''$  at constant low velocity named ‘E’ corresponds to the ridge of emission south-



**Fig. 4.** Longitudinal Position-Velocity diagram ( $PV_{\parallel}$ ) formed along the axis ( $PA=228^{\circ}$ ) with the source in  $y = 0$  and positive offsets toward SW. For the red-shifted lobe, and for each branch, the connected crosses correspond to the intersections of the ellipse fit in the channel maps with the axis, each family with a different color. For the A features, the subscript 0 (1) refers to the intersections of the side of the ellipses closer to (farther from) the source. Horizontal dotted lines mark the  $V_{\text{LSR}}$  of the channel maps in Fig. 3, vertical dotted lines the offsets  $y$  of the transverse PV diagrams shown in Fig. 5. The solid cyan line is at  $V_{\text{sys}}$ . The symbols in color indicate corresponding emission points in the diagrams of Fig. 5.

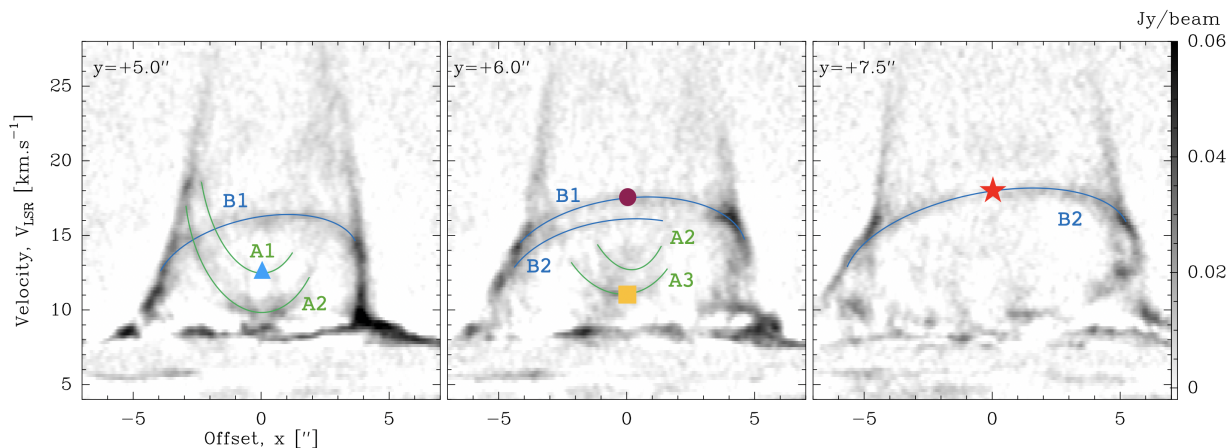


**Fig. 5.** Selection of transverse Position-Velocity diagrams ( $PV_{\perp}$ ) formed perpendicularly to the axis at separation  $y = 5''.0$ ,  $6''.0$  and  $7''.5$  from the source, and with orientation  $PA=318^{\circ}$  (i.e. positive offsets toward NW). The curves indicate corresponding substructures in Fig. 3 and 4. The symbols illustrate the fact that in a given diagram taken at offset  $y_n$  the point of coordinates  $(x=0, V_{\text{LSR}}=V_m)$  marks the emission along the axis, and, therefore, has a unique correspondance in the  $PV_{\parallel}$  diagram of Fig. 4 with the point at coordinates  $(y = y_n, V_{\text{LSR}}=V_m)$ .

west to the source and almost perpendicular to the flow direction seen in Fig. 1.

### 3.5. Transverse Position-Velocity diagrams

Appendix B presents an atlas of the transverse Position-Velocity diagrams (hereafter  $PV_{\perp}$ ) obtained for the red lobe with a  $0''.3$  wide virtual slit centered on the axis and oriented at  $PA=318^{\circ}$  (i.e. perpendicular to the axis and with positive offsets toward

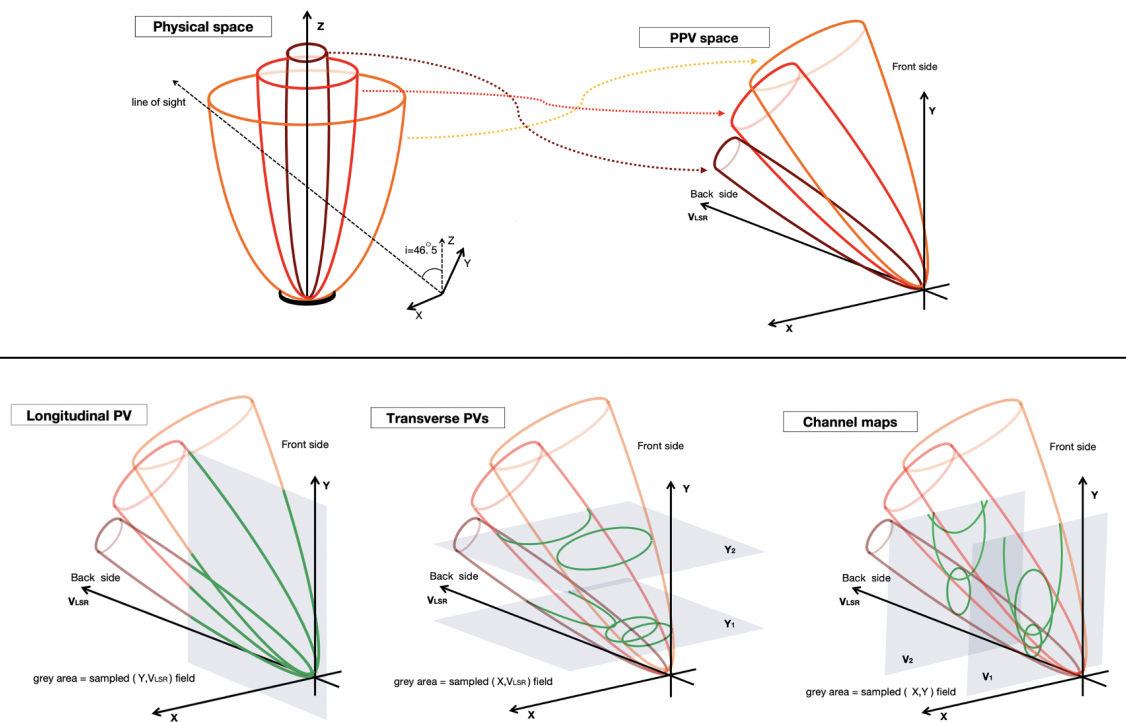


**Fig. 6.** Proposed structure of the wind derived from the data analysis, in the simplified case of no rotation of the flow. *Top*: the nested shells in the physical space (left) have progressively smaller radius, higher poloidal velocity and faster apparent acceleration as the axis is approached, so that the corresponding paraboloids in the position-position-velocity (PPV) space are progressively closer to and more inclined towards the velocity axis (right). *Bottom*: examples illustrating the origin of the structures seen in the orthogonal projections of the datacube.

NW), formed at separations  $y$  from  $3''.5$  to  $10''$  from the source, in steps of  $0''.5$ . Illustrative examples are given in Fig. 5, for selected separations from the star.

In all panels, the emission presents a bell shape around the  $x = 0$  axis, narrower toward high velocities. Progressing with separation from the source, the bell becomes wider, but the lateral 'walls' maintain coherence. Outside of the bell, low-velocity material ( $7.5 - 9.5 \text{ km s}^{-1}$ ) is present.

Internal structures in the form of arcs and elliptical curves are found in all the panels, with a monotonic increase in average velocity and size as the separation from the source increases. This behavior is reminiscent of the variation with velocity observed for the substructures in the channel maps and in the  $PV_{\parallel}$  diagram. Despite the additional difficulty due to the signal confusion created by stacking of the emission traces in the same velocity channel, Figure 5 proposes an identification of visible curves with features belonging to the A and B family, with the same labels and color code as in Fig. 4.

An evident characteristic of the structures identified in the transverse diagrams is the *inclination* with respect to the  $x = 0$  axis. This property is related to the rotation of the flow. The two opposite borders of the wind, in fact, present a velocity shift due to the projection of the rotation (i.e. toroidal) velocity along the line of sight. An illustration of this effect is offered in de Valon et al. (2022), Fig. 2. The observed features display higher red-shifted velocities on the NW side (seen more clearly for the curves of the B family) consistent with a clockwise rotation sense looking from the tip of the red lobe toward the source. This sense of rotation matches that of the disk (Garufi et al. 2021).

In summary, the ensemble of maps presented in this Section indicates that the orthogonal projections of the Position-Position-Velocity (PPV) datacube all show well-defined substructures, consisting of concatenated curves in the velocity channel maps and in the transverse  $PV_{\perp}$  diagrams, and of a fan of traces opening from the source region in the parallel  $PV_{\parallel}$ . The features can be connected from one projection to the other, and this leads to inferring the existence of coherent structures in the datacube. The most generic distribution of the emission that can justify the properties of the presented maps is a system of concatenated paraboloid-like surfaces in the datacube, with different inclinations with respect to the velocity axis. In the following Section we investigate which structure of the wind in physical space could give rise to the derived properties of the datacube.

#### 4. Interpretation of the substructures in terms of nested gas shells.

The distribution of the emission flux in the PPV space described above points to a wind configuration in physical space consisting of a number of rotating nested shells, gradually opening with distance from the source, and with the gas having progressively higher propagation velocity and larger apparent acceleration for shells closer to the axis. An illustration of this hypothesis is given in the sketch of Fig. 6, based on an axisymmetric flow composed of three such layers, which are assumed not to rotate for simplicity. In the real case, rotation and inclination introduce deformations of the traces in the projected maps. As mentioned above, flow rotation produces in the  $PV_{\perp}$  diagrams a tilt of the features with respect to the  $x = 0$  axis, with a larger skew for larger toroidal velocities. This effect is clearly detected for

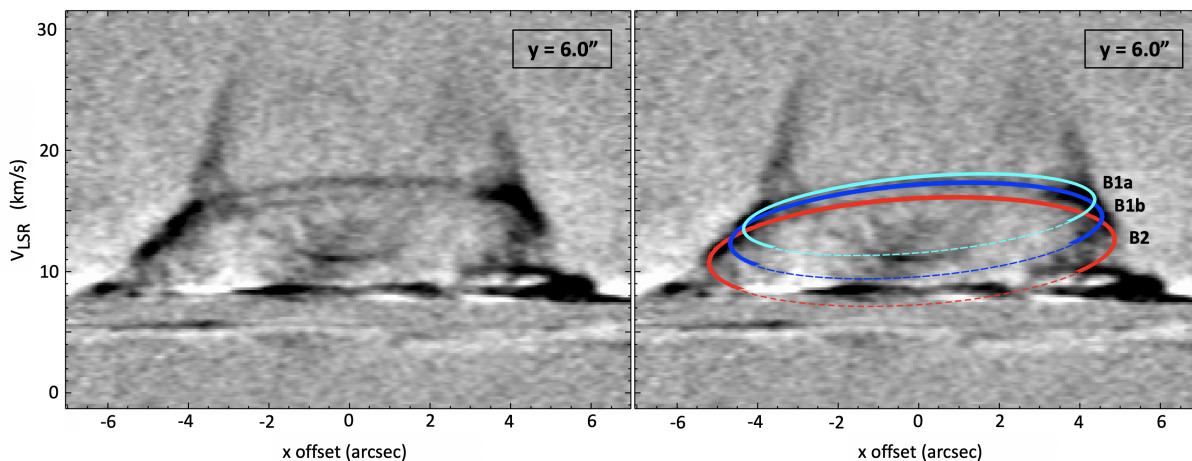


**Fig. 7.** Example of ellipse fit for the structures of family B, that is features B1 (decomposed in two twin intersecting features B1a, B1b) and B2, in the transverse  $PV_{\perp}$  diagram formed at offset  $y=6''$  from the source. The fit is anchored at the upper arc and at the lateral apexes of the features.

traces of family B, and indicates a rotation sense of the flow consistent with the one in the disk. On the other hand, inclination with respect to the line of sight produces a deformation of the closed curves in the  $PV_{\perp}$  diagrams with respect to the pure ellipse shape, as described, e.g., in De Valon (2021). For an inclination of about  $45^{\circ}$  as in the present case, the low-velocity part of the ellipses is expected to be flatter than the high-velocity part. However, this deformation is not easily recognized in our maps, as the structures centered at moderate velocity are faint and/or do not have a visible upper part, while those centered at low velocity have the bottom part hidden by the absorption due to the CO gas at  $V_{\text{sys}}$ .

However, in general, the data appear to support the interpretation of the observed substructures in terms of distinct rotating nested shells in physical space. As mentioned in the Introduction, the same hypothesis has been advanced for other molecular winds presenting similar spectro-imaging properties in high resolution data. Notably, however, HL Tau is the only object among the known cases with a detectable ring / gap structure in the disk. Thus, in this case, it is possible to investigate the relationship between the substructures observed in the wind and those seen in the disk.

#### 4.1. Tomographic reconstruction of the wind shells.

The series of  $PV_{\perp}$  diagrams (Fig. B.1) allows, in principle, a 'tomographic reconstruction' of the wind shells that provides information on their morphology and kinematics in the physical space. This can be done by measuring the width, inclination, and position of each detected feature in the subsequent diagrams. However, the task is obstructed by the confusion generated by the faintness of the signal and the stacking of structures at low  $V_{\text{LSR}}$ . The main difficulty resides in the uncertainty of the identification of a coherent feature to follow in its evolution from a diagram to the next. Nevertheless, we illustrate the principles of the analysis focusing on the features of family B, that are clearly identified and have a regular elliptical shape, over which the fit can be easily adjusted by eye. The analysis of the other fainter arcs requires a refined identification procedure, currently under development, and the results will be presented in the next paper of the series (Nony et al., *in prep*).

A closer inspection of both the parallel and transverse  $PV$  diagrams reveals that the B1 feature is actually composed of two intersecting curves that we label B1a and B1b. Therefore, in the example shown in Fig. 7, one finds the three ellipse fit. For each feature, the fit is anchored in the upper arc and at the lateral apexes, but not in the bottom arc. As mentioned above, the latter is difficult to identify due to stacking at low velocity, the intervening absorption of the signal, and the deformation due to the flow inclination. In any case, the coordinates of the apexes are sufficient to determine the local shell radius  $r$ , the toroidal velocity  $V_{\phi}\hat{e}_{\phi}$  and the axial velocity  $V_z\hat{e}_z$  (referring to a comoving cylindrical coordinate system centered on the star, with  $\hat{e}_z$  directed towards  $PA=228^{\circ}$ ).

In practice, if  $(x_{-,n}, V_{-,n})$  and  $(x_{+,n}, V_{+,n})$  identify the SE and NW apexes in the  $PV_{\perp}$  diagram at separation  $y_n$  from the source, then:

$$r_n = \frac{(x_{+,n} - x_{-,n})}{2}$$

$$V_{z,n} = \frac{(V_{-,n} + V_{+,n}) - 2V_{\text{sys}}}{2 \cos i} \quad V_{\phi,n} = \frac{(V_{+,n} - V_{-,n})}{2 \sin i} \quad (1)$$

where  $V_{\text{sys}} = +7.1 \text{ km s}^{-1}$  and  $i=46.5^{\circ}$ .<sup>2</sup> In addition, one can find the local tangent angle  $\alpha_n$  to the shell from the derivative of the best polynomial fit to the variation of  $r_n$  with  $z = y/\sin(i)$  (which turned out to be of the first order for B1a and B1b, and of the second order for B2). If the wind flows along the shell, the poloidal velocity  $V_p = V_r\hat{e}_r + V_z\hat{e}_z$  is tangential to the surface, and  $V_{p,n} = V_{z,n}/\cos(\alpha_n)$ . To validate this assumption, one should measure independently  $V_{r,n}$  and verify that  $V_{r,n}/V_{z,n} = \tan \alpha_n$ . Unfortunately, the measurement of  $V_r$  is complicated by the inclination of the flow with respect to the l.o.s. that distributes the information at displaced  $y$  offsets (see Fig. D.1), in regions where the emission traces are faint and/or confused. This makes the conditions for the test prohibitive in almost all cases. However, we could measure  $V_r$  and confirm the validity of the hypothesis at least for a few positions, as described in Appendix D. In the following, it is assumed that the flow streams along the shell surfaces.

<sup>2</sup> In writing these formulas we neglect flow wiggling and precession. A check on the validity of this assumption is reported in Appendix C.



**Table 1.** Properties of the features of family B measured in the transverse  $PV_{\perp}$  diagrams and derived outflow parameters.

	$y$ [arcsec]	$x_{-}$ [arcsec]	$x_{+}$ [arcsec]	$V_{-}$ [km s <sup>-1</sup> ]	$V_{+}$ [km s <sup>-1</sup> ]	$z$ [10 <sup>3</sup> au]	$r$ [10 <sup>2</sup> au]	$V_z$ [km s <sup>-1</sup> ]	$V_{\phi}$ [km s <sup>-1</sup> ]	$\alpha$ [deg]	$V_p$ [km s <sup>-1</sup> ]	$J = rV_{\phi}$ [10 <sup>2</sup> au km s <sup>-1</sup> ]	$r_0$ [au]	$\lambda_{\phi}$
B1a	4.5	-3.51	3.61	12.06	14.62	0.9	5.2	9.1	1.76	21.5	9.7	9.3	54	2.9
	5.0	-3.85	3.80	12.21	14.75	1.0	5.6	9.3	1.75	21.5	10.0	9.9	56	3.1
	5.5	-4.08	4.07	12.84	15.51	1.1	6.0	10.3	1.84	21.5	11.0	11.0	56	3.4
	6.0	-4.38	4.38	13.43	15.99	1.2	6.5	11.1	1.76	21.5	11.9	11.4	54	3.6
	6.5	-4.68	4.57	13.46	16.01	1.3	6.8	11.1	1.76	21.5	12.0	12.0	56	3.7
B1b	4.5	-3.72	3.67	10.90	13.33	0.9	5.4	7.3	1.67	24.1	8.0	9.1	64	2.6
	5.0	-4.02	3.86	11.36	13.95	1.0	5.8	8.1	1.79	24.1	8.8	10.4	66	3.0
	5.5	-4.31	4.16	11.85	14.37	1.1	6.2	8.7	1.74	24.1	9.6	10.8	64	3.1
	6.0	-4.70	4.55	12.14	14.63	1.2	6.8	9.1	1.72	24.1	10.0	11.7	66	3.3
	6.5	-5.22	4.77	12.04	14.63	1.3	7.4	9.1	1.79	24.1	9.9	13.1	74	3.6
B2	6.0	-5.25	4.92	10.58	12.58	1.2	7.5	6.5	1.38	19.9	6.9	10.3	84	2.6
	6.5	-5.57	5.26	11.00	13.19	1.3	8.0	7.3	1.51	19.3	7.7	12.0	89	3.0
	7.0	-5.72	5.55	11.51	13.79	1.4	8.3	8.1	1.57	18.7	8.5	13.0	87	3.2
	7.5	-5.92	5.63	11.93	14.26	1.5	8.5	8.7	1.61	18.1	9.2	13.7	84	3.5
	8.0	-6.21	5.73	12.16	14.47	1.6	8.8	9.0	1.59	17.4	9.5	14.0	83	3.6
	8.5	-6.59	5.97	12.19	14.40	1.7	9.3	9.0	1.52	16.8	9.4	14.1	84	3.6
	9.0	-6.94	6.09	12.16	14.34	1.8	9.6	8.9	1.50	16.2	9.3	14.4	87	3.6
	9.5	-7.09	6.32	12.21	14.40	1.9	9.9	9.0	1.51	15.5	9.4	14.9	89	3.7
	10.0	-7.13	6.47	12.50	14.72	2.0	10.0	9.5	1.53	14.9	9.8	15.3	87	3.8

**Notes.** Listed parameters, from left to right: (1) feature name as identified in Fig. 7; (2) offset from the source of the considered  $PV_{\perp}$  diagram; (3,4)  $x$  coordinates of the SE and NW apices of the ellipse fit; (5,6)  $V_{\text{LSR}}$  velocity at the SE and NW apices; (7) offset from the source  $z = y / \sin i$  deprojected along the flow axis ( $i=46.5^{\circ}$ ); (8,9,10) shell radius  $r$ , axial velocity  $V_z$ , toroidal velocity  $V_{\phi}$  derived from Eq. (1); (11) local tangent angle to the shell derived from the derivative of the polynomial fit of  $r = r(z)$ ; (12) poloidal velocity  $V_p = V_z / \cos \alpha$ ; (13) specific angular momentum  $J = rV_{\phi}$ ; (14) shell footpoint calculated from Eq. (3), with average values 55, 67 and 86 au for B1a, B1b and B2, respectively; (15) component  $\lambda_{\phi} = rV_{\phi} / r_0^2 \Omega_0$  of the magnetic lever arm  $\lambda$  in Eq. (2). The uncertainty estimated from the spatial and spectral resolution is about 5% on  $r$  and about 10% on  $V_z$  and  $V_{\phi}$ . The dependency on the angle  $\alpha$  limits the accuracy on  $V_p$  to 15%. Error propagation leads to an uncertainty of about 15% for  $J$ . The uncertainty on  $r_0$  and  $\lambda_{\phi}$  is estimated to be about 20%, from the sensitivity to variations of the input parameters in Eq. (3).

The parameters derived from the fit for the  $y$  offsets in which the B substructures are well identified are given in Table 1 and are illustrated in Fig. 8. The three shells turn out to have a similar trend for the radius, that increases from about  $5 \cdot 10^2$  to  $10^3$  au for distances from  $10^3$  to  $2 \cdot 10^3$  au from the star, and appear indeed to be nested, with B1a the innermost one and B2 the external layer. The smaller opening angle of B2, determined at larger separations from the star than for B1, suggests recollimation at large distances. The axial velocity, between 6 and  $11 \text{ km s}^{-1}$  at the sampled distances, is higher for the inner shells. In shell B2, after a steep increase in the first positions, a plateau is found after  $1.5 \cdot 10^3$  au, and a similar plateau appears to be reached also in B1a and B1b, but closer to the source, at  $1.3 \cdot 10^3$  au. The poloidal velocity, almost proportional to  $V_z$ , shows a similar trend. The toroidal velocity  $V_{\phi}$  is constant on average along a single shell, but is progressively lower toward the outer layer, with an average of  $1.77$ ,  $1.74$  and  $1.52 \text{ km s}^{-1}$ , for B1a, B1b and B2, respectively. The specific angular momentum  $J = rV_{\phi}$  varies between 900 and  $1500 \text{ au km s}^{-1}$ . Its value increases monotonically in the B1a, B1b shells. For the B2 shell, sampled at larger separations from the source, a knee is observed at  $1.5 \cdot 10^3$  au.

## 5. Discussion

As mentioned in the Introduction, different scenarios have been proposed for the interpretation of the recent observations of layered molecular winds. These scenarios are, in principle, also ap-

plicable to the HL Tau case. Ellipses in channel maps and transverse PVs, as well as an increase in velocity in longitudinal PVs are predicted by models of magnetized disk winds (Ray & Ferreira 2021; de Valon et al. 2022), models of wide-angle winds driven by swept-up shells (Lee et al. 2000; Zhang et al. 2019), unified models with a jet-bearing wide-angle X-wind (Shang et al. 2023; Ai et al. 2024). On the other hand, flow rotation is expected in both magnetically driven winds, which extract angular momentum from the disk, and thermal photoevaporative winds (Alexander et al. 2014), which conserve their initial angular momentum. The layered wind structure could also be due to the interaction with a pulsed axial jet (e.g., Rabenahary et al. (2022)). Each of these possibilities deserves a dedicated analysis. In the following, we focus on the extended MHD disk wind (DW) scenario, deferring the comparison of the observed trends with other classes of models to forthcoming papers.

### 5.1. Basics of the MHD Disk-Wind theory.

According to the Disk-Wind scenario, a young star-disk system is embedded in a large-scale hourglass-shaped, twisted magnetic field inherited from the collapse of a magnetized rotating cloud. In this configuration, and provided sufficient ionization, a wind can be launched by the action of magnetic effects from the surface of the rotating disk. The outflow carries away vertically angular momentum, and the consequent braking of the disk rotation allows accretion through the disk to occur. Self-similar

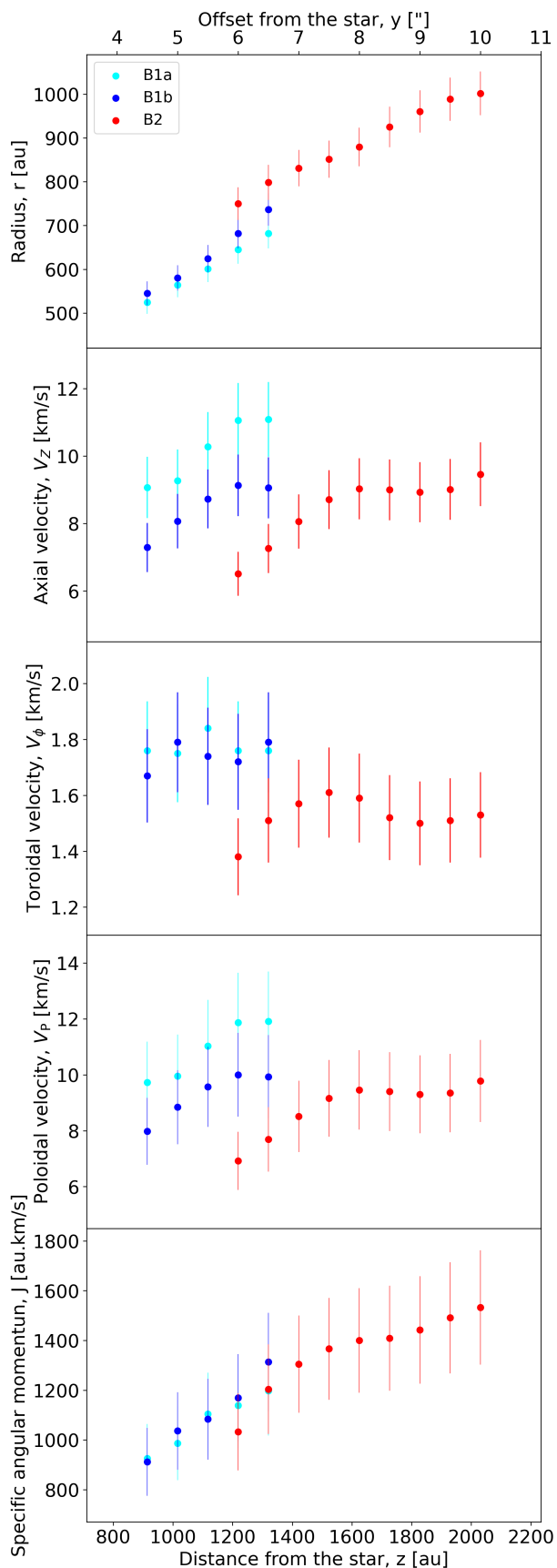


**Fig. 8.** Variation of physical parameters in the shells B1a (cyan), B1b (blue) and B2 (red) with distance from the source as derived from the tomographic analysis of the  $PV_{\perp}$  diagrams in Section 4.1, and reported in Table 1.

steady and axisymmetric DW solutions in ideal MHD conditions have proven to be successful in reproducing the observed properties of the axial atomic jets (see, e.g., Frank et al. 2014; Pascucci et al. 2023). The wind structure predicted by such models, that is, nested rotating gas shells, with higher poloidal velocities measured for the inner shells, is actually observed also in the outer CO outflows, as shown above for the HL Tau case. However, to properly describe global disk winds from an extended launch region, the models have to include non-ideal effects in the disk. Among them, ambipolar diffusion (AD) between neutrals and ions becomes dominant when the ionization is scarce (e.g. Pinto et al. (2008)). Magnetized winds also arise in this case, as described, e.g. in the review by Lesur et al. (2023).

An important quantity of the DW theory is the parameter  $\lambda$ , which represents the ratio between the extracted and the initial specific angular momentum. Following the definition of Blandford & Payne (1982),  $\lambda$  can be expressed as:

$$\lambda = L/\Omega_0 r_0^2 = \frac{\Omega r^2}{\Omega_0 r_0^2} - \frac{r B_{\phi} B_p}{\Omega_0 r_0^2 4\pi \rho V_p} \quad (2)$$

where  $L$  is the total specific angular momentum carried away by the MHD wind along a streamline, in the form of both matter rotation and magnetic torsion.  $\Omega_0$  is the Keplerian angular rotation speed at the launch point  $r_0$ , and  $\rho$ ,  $B_p$  and  $B_{\phi}$  are the volume density and the poloidal and toroidal components of the magnetic field in the wind. The higher the value of  $\lambda$ , the more efficient is the extraction of angular momentum and the acceleration of the wind. The parameter  $\lambda$  is often referred to as the ‘magnetic lever arm’, as it can be expressed as  $(r_A/r_0)^2$ , where  $r_A$  is the Alfvén radius, that is the cylindrical radius at which the poloidal velocity reaches the Alfvén velocity  $V_A = B_p/(4\pi\rho)^{1/2}$ . The locus of points in the wind where this occurs is called Alfvén surface, and it indicates the region above the disk where the increasing inertia of the flow starts to overcome the magnetic push. In the self-similar steady DW solutions this surface has a conical shape.

In the DW scenario  $\lambda$  is constant along a streamline, meaning that the angular momentum is gradually transferred from the magnetic field to the motion of the particles. Proceeding along the streamline, the component  $\lambda_{\phi} = \Omega r^2/\Omega_0 r_0^2$ , representing the normalized specific angular momentum, increases, and approaches  $\lambda$  in the asymptotic regime, in which the magnetic contribution is sensibly reduced. The distance from the disk at which this occurs is larger for higher values of  $\lambda$ , and can be several orders of magnitude higher than the altitude of the Alfvén surface. However,  $\lambda_{\phi}$  may never reach  $\lambda$ , as the magnetic structure maintains asymptotically a fraction of the available energy.

The importance of gas pressure versus magnetic effects in the disk can be parametrized by the plasma  $\beta$  at the midplane, defined as  $\beta = 8\pi\rho_0 c_s^2/B_0^2$ , where  $c_s$  is the sound speed and  $\rho_0, B_0$  are the mean density and vertical magnetic field threading the disk. Unfortunately, the magnetic field amplitude in the disk is not available from observations. However, according to theoretical studies for self-similar disk wind solutions,  $\lambda$  is expected to increase with smaller  $\beta$  (e.g. Jacquemin-Ide et al. 2019; Lesur 2021). It follows that the determination of  $\lambda$  from the observations is crucial not only to identify the properties of the wind, but also to constrain the importance of magnetic effects in the disk.

Self-similar DW solutions from fully turbulent disks have been found for a wide range of  $\lambda$  values at both high and low  $\beta$  (Ferreira 1997; Casse & Ferreira 2000a; Jacquemin-Ide et al. 2019; Zimniak et al. 2024). On the other hand, in disk regions where the ionization is quenched in the midplane, as expected in

the so-called disk 'dead zone', solutions are dominated by AD, and low values of  $\lambda$  have been found, up to about 3 (Lesur 2021). Recent results show that the dead zone could actually start closer than 1 au from the star in T Tauri disks (Flock et al. 2019), and extend to the outer disk regions of interest here.

In the next Section the principles of the DW theory will be applied to the derivation of relevant quantities in the HL Tau wind, such as the location of origin of the flow in the disk, and the magnetic lever arm. The variation with distance from the source of the wind parameters will also be tested against the prescriptions of the models.

## 5.2. Derivation of the shell footpoints in the Disk Wind scenario.

Regardless of the conditions adopted for the disk physics, the wind can be treated in ideal MHD. Assuming that the flow is a cold stationary and axisymmetric disk wind, from the measurements described in Sect. 4.1 one can infer the so-called footpoint radius  $r_0$ , that is, the radius of the disk annulus from which the wind shell originates. Following the method introduced in Bacciotti et al. (2002) and refined in Anderson et al. (2003),  $r_0$  can be found as the real solution of the following third-order equation:

$$rV_\phi(GM_\star)^{1/2}r_0^{-3/2} - 3/2(GM_\star)r_0^{-1} - (V_p^2 + V_\phi^2)/2 = 0, \quad (3)$$

where  $G$  is the gravitation constant and  $M_\star$  the mass of the central source. The equation is valid if the enthalpy and the gravitational force exerted by the star are negligible with respect to the kinetic terms at the height above the disk where the wind parameters are measured. These conditions are fulfilled for cold CO molecular flows with poloidal velocities around 10 km s<sup>-1</sup> observed at more than 500 au from a star of solar type, conditions met in our case.

The results obtained by applying the calculation to the features of family B are collected in column (14) of Table 1. For each shell, the footpoint radii derived from the measurements at different separations from the star cluster around a single value with a spread of only a few au. The uncertainty of ~20% reported in the table was estimated by testing the sensitivity of the calculation in Eq. (3) to variations of the input parameters as large as their respective errors. The average footpoint radii are thus 55±10 au for shell B1a, 67±13 au for shell B1b and 86±15 au for the B2 shell. With the adopted stellar mass of 2.1 M<sub>⊙</sub>, the Keplerian velocity at these distances is 5.8, 5.3 and 4.7 km s<sup>-1</sup>, respectively.

An equivalent derivation of the shell footpoints is illustrated by the diagnostic diagram of Fig. 9, constructed following the procedure described in Ferreira et al. (2006). Under the same assumptions, in fact, it can be shown that  $J$  and  $V_p$  for a given streamline depend only on the two parameters  $r_0$  and  $\lambda_\phi$ . The curve grid at constant  $r_0$  and  $\lambda_\phi$  is drawn in Fig. 9. The location of the measured ( $J$ ,  $V_p$ ) values in this diagram gives estimates of the radius of the footpoint  $r_0$  and of the parameter  $\lambda_\phi$  by comparison with the theoretical curves.

In HL Tau, for each individual shell the points lie on the corresponding  $r_0$  curve, progressing to higher values of  $\lambda_\phi$  as the distance from the source of the corresponding PV<sub>⊥</sub> diagram increases. As discussed in the next section, this trend is consistent with the one expected in a DW scenario.

The derived footpoint radii are larger than our spatial resolution limit ( $d = 40$  au). In fact, with reference to Fig. A.1, the base of the red-shifted wind appears resolved in the channel maps at low velocities between  $V_{\text{LSR}} = 7.4$  and 9.4 km s<sup>-1</sup>. However, the

emission pattern is not clear in these maps, as contributions at low velocity and close to the star may come both from the outflow base and from parts of the envelope, possibly from accreting streamers, or from some part of the disk. However, this velocity interval is consistent with that in which, under the DW hypothesis, we expect to resolve the flow base in these observations. This point is discussed in Appendix A. In the channel maps at  $V_{\text{LSR}} > 9.5$  km s<sup>-1</sup> the wind base is not resolved on the SE side (the emission peak on the NW side of the source corresponds to the receding side of the disk). At this velocity the flow appears to originate within a region inside the resolution limit of 40 au, it propagates initially with a large opening angle, up to a projected distance of about 0."5 from the disk, and then it appears to recollimate. This trend is again consistent with the DW scenario, following which the inner shells coming from an unresolved footpoint distance are subject to a faster acceleration, have an initial large opening angle, which then reduces to the collimated value (cf. Fig. 10, first panel).

Interestingly, the footpoint values obtained are found to be in the region in which the outermost rings of dust are observed (ALMA Partnership et al. 2015; Stephens et al. 2023). In particular, the footpoint of the B2 shell coincides with the position of a clearly detected ring of dust with peak emission at about 86 au, while the other two shells have footpoints falling in a region less clearly defined, on the outer edge of a progressively fainter shoulder of the dust emission. In this region Stephens et al. (2023) actually identify a couple of very shallow gaps at 53 and 68 au<sup>3</sup>.

However, we caution that, in addition to taking into account the 10-15 au uncertainty of the measurements, one should consider that the positions of the wind footpoints should actually be compared with the distribution of disk substructures *in the gas*, rather than in the dust, and these may not coincide. It is well known that bumps in the gas pressure act as dust traps, but the average shift of the peak positions of gas pressure and dust emission depends on the model adopted (see, e.g. Riols et al. 2020; Hu et al. 2022).

Yen et al. (2019a) reports profiles of gas emission in the HL Tau disk in the molecular lines of HCO<sup>+</sup>(3-2) and HCO<sup>+</sup>(1-0). The profiles are quite shallow, with no clear substructure detected, but it is interesting to note that all the B-shell footpoints coincide with peaks in the HCO<sup>+</sup>(3-2)/HCO<sup>+</sup>(1-0) ratio (see their Fig. 9), which, under the assumption of constant temperature, can be considered proportional to the gas density. According to this comparison, therefore, *the wind shells appear to arise from gas rings*. However, the association of the footpoint locations with rings remains tentative at this stage, as a more reliable identification would require higher precision in the measurements of the positions of both the shell footpoints and of the disk substructures in the emission of the gas tracers.

## 5.3. Variation of parameter $\lambda_\phi$ in the wind shells

In Section 5.2,  $\lambda_\phi$  at each sampled distance from the source has been determined through its direct calculation as in Table 1, or graphically as in the diagram of Fig. 9. For all points relative to HL Tau  $\lambda_\phi$  is within the range  $\lambda_\phi = 2.5$ -3.8, and for each shell, the points relative to the PV<sub>⊥</sub> at subsequent offsets follow curves at constant  $r_0$ , progressing toward higher values of  $\lambda_\phi$  as the distance from the source increases. Notably, the same behavior is shown by the points corresponding to theoretical DW models, in

<sup>3</sup> Note that ALMA Partnership et al. (2015) adopt a distance of HL Tau of 140 pc, while Stephens et al. (2023) adopt 147.3 pc, as in our work.

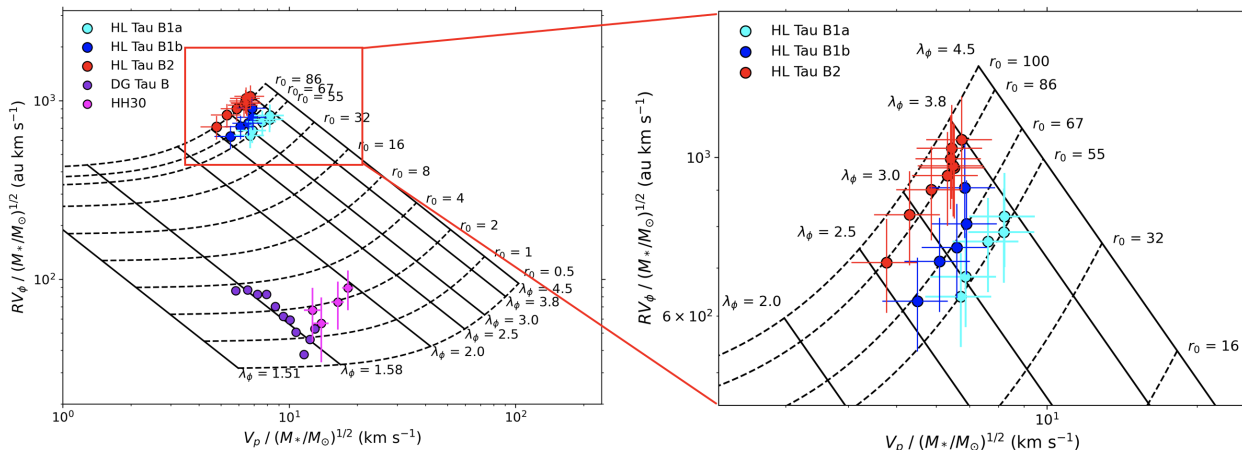


**Fig. 9.** Footpoint radii  $r_0$  and parameter  $\lambda_\phi = \Omega r^2 / \Omega_0 r_0^2$  determined for the B1a, B1b and B2 shells following the diagnostic procedure in Ferreira et al. (2006). The diagram also reports the results for the wind from DG Tau B (de Valon et al. 2022), and for the wind from HH 30 (Louvet et al. 2018; López-Vázquez et al. 2024), that, however, are derived with a different selection of the input data (see text).

a zone in which the asymptotic regime has not yet been reached (see Appendix E). This appears to indicate that also in HL Tau we are probing a transition region in which the magnetic field is still transferring angular momentum to the matter.

Anyhow, the clustering of the points for B2 seems to indicate that the distances probed are not far from the asymptotic regime. This point should be farther away for the outer streamlines than for the inner ones, due to the self-similar nature of the flow (Ferreira et al. 2006). This is in line with the fact that a given value of  $\lambda_\phi$  is attained closer to the star for the B1 shells with respect to B2.

We also show in Fig. 9 the values of  $J$  and  $V_p$  derived for the shells identified in the HH30 CO outflow (Louvet et al. 2018; López-Vázquez et al. 2024) and in the bright conical DG Tau B CO outflow (de Valon et al. 2022). In these two cases, each couple of  $(J, V_p)$  values corresponds to an average along a given shell. Interestingly, the  $J$  and  $V_p$  measurements in HH 30 follow a curve at roughly constant  $r_0$ , while the points in DG Tau B follow a curve at constant  $\lambda_\phi$ . This latter behavior is expected in the case where each shell is probing a flow surface of varying  $r_0$  in the same extended disk wind solution. Averaging the  $(J, V_p)$  values along the shells in HL Tau would lead to a trend similar to the one observed in DG Tau B although with larger values of  $\lambda$  and  $r_0$ .

#### 5.4. Comparison with self-similar MHD disk-wind solutions.

The quantity  $\lambda_\phi$  is only one component of the magnetic lever arm. To find observationally the value of  $\lambda$  with the methods described above, one should examine the wind in the shell until the point at which asymptotically  $\lambda_\phi \sim \lambda$ . However, this is hampered by the progressive weakness of the signal and by the interaction of the flow with the environment. A possible solution is to compare the variation of the wind parameters in the three shells with the trends prescribed by the DW models calculated for different values of  $\lambda$ . This also constitutes a test of the validity of the application of the DW theory to the observed outflow.

We do not attempt to explore the full range of possible self-similar solutions, but we show expectations from only three wind models. Turbulence-dominated disc models should be used for MHD winds anchored below a few au, and AD-dominated mod-

els further out. However, in both cases, the MHD wind is described by the same set of ideal MHD equations, and what differs is only the physical conditions at the jet launching point. The main constraint used here will therefore be the fact that our wind models must encompass the range of  $\lambda$  values compatible with the observations.

We use two solutions, L1 and L2, corresponding to cold disk winds arising from an AD dominated disk (Lesur 2021), with, respectively,  $\beta = 10^5$  and  $\beta = 63$  and corresponding to  $\lambda = 1.56$  and  $\lambda = 2.76$ . Both solutions assume an ambipolar diffusion parameter  $A_m = 1$  and no Ohmic diffusion. The disc and its atmosphere were assumed to be cylindrically isothermal (sound speed  $c_s(R, z) = c_s(R, z = 0)$ ), with a disc aspect ratio  $\epsilon = h/R = 0.1$  (where  $h$  is the geometric thickness of the disk  $h = c_s(R, z = 0) / \Omega_K(R)$ , with  $\Omega_K(R)$  the Keplerian angular velocity). The  $\lambda$  value achieved by solution L2 is the highest published so far for AD-dominated disks.<sup>4</sup>

In order to represent a MHD wind with a higher magnetic lever arm, we use a warm solution computed in the case of a fully turbulent disc, similar to the solution presented in Tabone et al. (2020) to reproduce the ALMA observations of the rotating SO wind in HH212. Our solution N5 describes a wind that arises from a thinner disk with  $\epsilon = 0.01$ ,  $\beta \sim 10$ , an effective magnetic Prandtl number of 1, a turbulence parameter  $\alpha_m = 2.3$ , a turbulence anisotropy  $\chi_m = 4.2$  and no turbulent pressure ( $\alpha_p = 0$ ) (Zimniak et al. 2024). Despite its large magnetic field, the ejection efficiency is high and the resulting outflow is dense. It achieves a magnetic lever arm  $\lambda = 5.64$  thanks to additional heating at the base of the wind (see the description in Casse & Ferreira 2000b). This heating is localized at the disk surface, and requires only 2% ( $f = 0.02$ , see their Eq. 25) of the dissipated power within the disk. Further up, the wind becomes adiabatic.

The comparison with the models is illustrated in Fig. 10. The points relative to the three B shells, with the same color code as in Fig. 8, describe the wind parameters normalized by their respective average footpoint radius  $\bar{r}_0$  and by the corresponding Keplerian velocity  $\bar{V}_K = V_K(\bar{r}_0)$ . The bottom curves are from the wind model from the AD-dominated disk region in Lesur

<sup>4</sup> The solutions in Lesur (2021) used in our work are freely available at <https://github.com/glesur/PPDwind>.

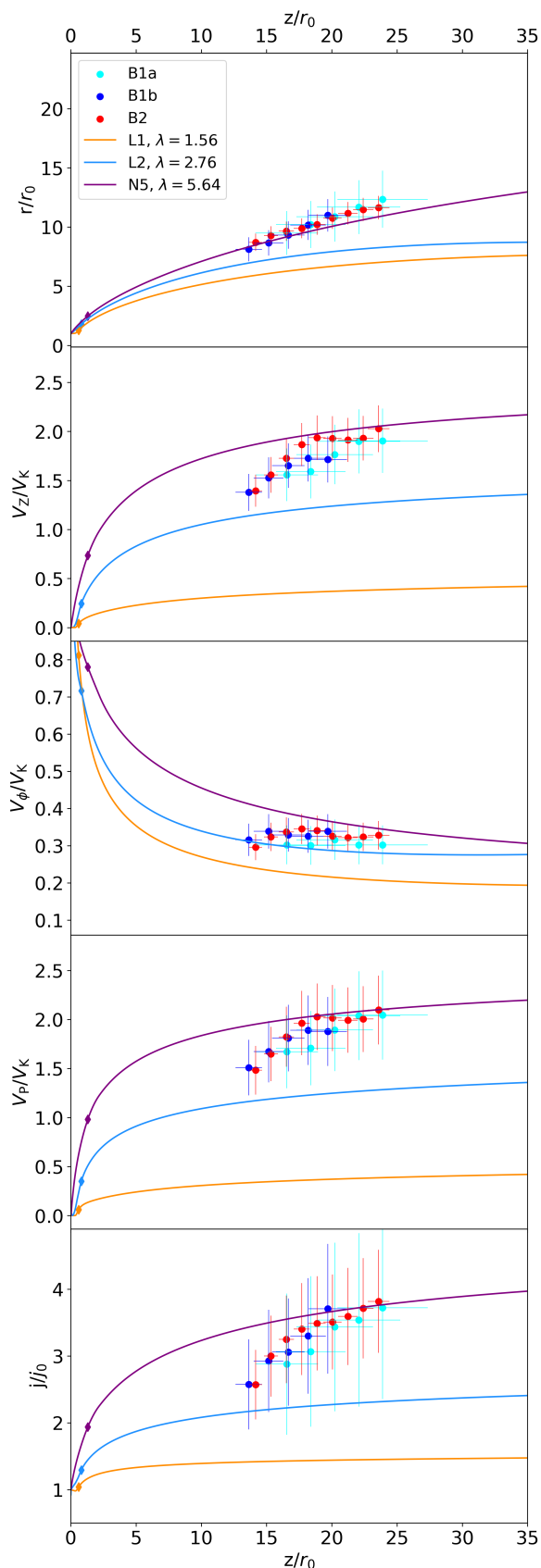


**Fig. 10.** Symbols: parameters for the shells B1a, B1b and B2 as in Table 1, normalized by the average  $r_0$  and  $V_K(r_0)$  of each shell. Curves: trends predicted by the models L1 ( $\lambda=1.56$ , orange) and L2 ( $\lambda=2.76$ , blue) of winds from an AD-dominated disk region, and by the model N5 ( $\lambda=5.64$ , purple) of a wind from a fully turbulent disk region (see text). The diamonds indicate the altitude at which the streamline crosses the corresponding Alfvén surface.

(2021), with curve L1 (orange) corresponding to the solution for  $\beta = 10^5$ ,  $\lambda=1.56$ , and curve L2 (blue) for  $\beta = 63$ ,  $\lambda=2.76$ . The upper curve N5 (purple) corresponds to the model of wind from a fully turbulent disk region that provides  $\lambda=5.64$  (cf. Zimniak et al. 2024).

First, it can be noted that once normalized, the points for the three observed shells in each panel nicely overlap within the errors. This is expected for self-similar solutions, in the case in which  $\lambda$  is similar for all shells. Secondly, the values of the normalized data are in the same range as those predicted by the models. The trends are similar to those expected from the models in the sampled range, but the gradient in the data points appears to be steeper than in the theoretical curves, for all quantities except  $V_\phi$ .

The top panel shows the comparison with the expected radius of the shells. The opening angle of the wind appears to be consistent with that predicted by the model N5 at higher  $\lambda$ . For the other quantities, the observed points lie in an intermediate position between the curves predicted by the two models L2 and N5, corresponding to an expected asymptotic value of  $\lambda$  between about 4 and 5 and  $\beta$  between 63 and 10.

The fact that the observational points lie between the two types of solution may have interesting implications. For winds coming from disk regions dominated by turbulence, the usual assumptions lead to a limiting anchoring radius of a few au, so in principle our observations, indicating larger footpoint radii, should be better described by the L solutions, corresponding to winds arising from AD-dominated disk regions.

On the one hand, this may indicate that the plasma  $\beta$  in the outer regions of the HL Tau disk is larger (that is, the magnetic effects are more important) than that commonly assumed for this zone in protoplanetary disks. In this case, a stronger field produces stronger vertical compression and a reduced wind density, which leads to a larger  $\lambda$ . However, other effects enter the wind acceleration mechanism, such as the disc aspect ratio, the existence of heating at the disc surface, the amount of effective turbulence, the degree of diffusion anisotropy, and the amount of ambipolar diffusion present in the disk. Regarding the last point, in HL Tau we might witness a case where ambipolar diffusion is much stronger in the disk than what is assumed in solutions of type L. This would effectively reduce the mass loading on the field lines and increase  $\lambda$  (Lesur 2021). Stronger ambipolar diffusion would imply a lower level of ionization in the disk than commonly assumed. An explanation for this could be the screening of cosmic rays by magnetic mirroring from the wind, as proposed from chemical arguments in the TW Hya disk by Cleeves et al. (2015). Since cosmic rays are the dominant ionization process at 50 au, reducing the amount of irradiation from these energetic particles could have a considerable effect and lead to an increase of  $\lambda$  for AD-dominated solutions, up to the values suggested by the observations. An AD-dominated scenario, leading to a laminar-type configuration in the disk region where rings/gaps are observed, would also be in line with the fact that rings appear to be remarkably axisymmetric in HL Tau, pointing towards a low level of turbulence (Pinte et al. 2016). However, a full quantitative exploration of all these aspects goes beyond the purpose of this paper and will be considered in future analyses.

In summary, the physical properties of the CO molecular wind from HL Tau appear to be compatible with a description in terms of a magnetized disk wind arising from a large region of the disk, up to 90 au and possibly more. The notion that not only the atomic axial jet originated in the first few au from the star, but also the outer wind may have a magnetic nature implies

that the feedback from the flows on the disk may occur up to large scales, which bears important consequences for the models of disk evolution and planet formation. First of all, such winds may be able to sustain accretion along the disk surface also at large distances from the star, in regions where the disk is internally weakly ionized and MHD turbulence, and hence viscous accretion, is suppressed. Other effects, however, may come into play. As discussed in Pascucci et al. (2024), for example, magnetically driven winds can slow the drift of solids in the direction of the star and affect the migration of planetary embryos.

### 5.5. Implications of the observed separation of the shells.

Up to this point, the discussion has regarded observational trends *along* the direction of the wind streamlines, and it has suggested an overall agreement with a DW scenario. However, puzzling evidence arising from the data is the inhomogeneity of the wind *across* its width, as indicated by the presence of distinct nested shells with enhanced emission. This property, not expected in a standard self-similar DW, is actually found in many molecular outflows observed at the high spatial and spectral resolution offered by ALMA (e.g. Zhang et al. 2019; Fernández-López et al. 2020; López-Vázquez et al. 2024; Ai et al. 2024; de Valon et al. 2020, 2022; Omura et al. 2024; Nazari et al. 2024, cf. Introduction).

The analysis of the HL Tau wind offers the advantage of allowing a comparison between the structures in the wind and in the disk. The derived configuration of the wind shells, the large estimated footprint radii, and the indication of origin of shells of higher emission in denser gas rings of the disk support recent models that prescribe the spontaneous formation of a ring-gap substructure in the disk, and of a connected inhomogeneous wind, as a result of magnetic instabilities (Béthune et al. 2017; Suriano et al. 2018, 2019; Riols & Lesur 2019; Riols et al. 2020; Cui & Bai 2021; Hu et al. 2022). In these numerical studies the secular evolution of protoplanetary disks is studied including ambipolar diffusion in the generalized Ohm's equation. As a result, one sees the rapid development of a self-organization of the magnetic field in the disk, which accumulates in the regions of lower mass density. In this way a system of rings and gaps forms quickly in the disk, with a greater concentration of magnetic field in the gaps. The final configuration also sees the formation of a transversely inhomogeneous disk wind arranged in nested shells, with alternate layers of enhanced density originating from the gaseous disk rings, and layers of faster lighter flow originating from the highly magnetized gaps. The ALMA observations like the ones described in this paper provide maps of the intensity of the line emission, and hence are prone to detect the wind layers of higher density, that is, in the above scenario, the layers arising from the disk rings.

The interest of this approach is the alternative it offers to models in which the disk substructure is due to the presence of young planets. Given the lack of detection of planetary bodies in structured disks (exception is made for PDS70, where, however, the planets reside in a very large cavity, Keppler et al. 2018), the point is of crucial importance, as it indicates that magnetic effects must be taken into account in the investigations aimed at the determination of the timescale of formation of the planets themselves.

However, a number of issues need to be addressed before we can confirm the validity of the proposed association. First of all, the value of the magnetic lever arm assumed in this class of numerical models is generally  $\leq 2$ . A similar simulation for  $\lambda \sim 4 - 5$ , as suggested by our analysis, would be desirable.

Secondly, the vertical extension of the structuration of the flow varies among the models, but in general the simulations do not reach the region at  $10^3$  au from the star in which we observe the wind structures with ALMA. An extension of numerical studies to large vertical scales would be needed, but it would come at the expense of a consistent computational effort. Finally, in these simulations, the disk structures are often seen to slowly move (Suriano et al. 2019; Martel & Lesur 2022), questioning the survival of their connection to the wind. However, the motion occurs on secular timescales, suggesting that the coherence of the magnetic flux tubes is probably not disrupted. Clearly, the applicability of the proposed structured disk/flow scenario to the observed cases needs to be tested with refined theoretical analyses, which, however, are out of the scope of the present work.

## 6. Conclusions

We investigated the properties of the molecular CO wind associated with the young HL Tau system by means of a detailed spectro-imaging analysis of the  $^{12}\text{CO}$  (2-1) line emission, observed at  $\sim 0''.28$  angular resolution in the context of the ALMA-DOT campaign (Podio et al. 2020a; Garufi et al. 2021). Our analysis confirms previous results derived from integrated intensity maps, but new insights on the structure of the flow come from the inspection of the individual projections of the Position-Position-Velocity (PPV) ALMA datacube in the brighter and less perturbed red-shifted lobe.

A complex substructure is revealed in the velocity channel maps, constituted by concatenated bubble- and arc-shaped features that progressively increase in size and distance from the source with velocity. The apparent conical shape of the wind appears to be the result of superposition of the limb-brightened borders of these features. The position-velocity (PV) diagram formed along the system axis presents a fan of separated almost linear traces opening from the source region, and with increasing velocity with offset from the star. The traces have strict spatial correspondence with the arcs in the channel maps. Finally, PV diagrams taken across the flow at stepped separations from the source show a series of concatenated ellipse-shaped features, that have a direct correspondance with the traces in the longitudinal PV diagram. The ellipses are tilted with respect to the system axis, indicating rotation of the flow in clockwise direction looking from the SW lobe toward the star, which matches the disk rotation sense.

On the basis of these projections we infer a global structure of the emission in the PPV datacube consisting of a series of distinct concatenated paraboloid-like surfaces with the apex toward the source, with progressively larger aperture as the angle of their axis with respect to the velocity axis increases (cf. Fig. 6). In the 3D physical space this translates into a finite number of coaxial, distinct, rotating nested gas shells. Ellipse fitting of the three directly identifiable structures in adjacent transverse PV diagrams allows a tomographic reconstruction of the morphology and kinematics of the outer three shells of the flow. We find smaller radii, higher poloidal and toroidal velocities, and fastest acceleration for shells progressively closer to the system axis.

This structure can be reproduced by a number of different wind acceleration mechanisms. In this paper, we focus on an analysis of the applicability of magnetohydrodynamic (MHD) disk winds (DW) accelerated from an extended region of the disk surface. We defer the comparison with other classes of models to future investigations.

Under the DW hypothesis, we derive from the rotation properties that the shells are rooted in the disk at 55, 67 and 86 au from the star, with an uncertainty of 20%. Interestingly, the shell footpoints are found in the region in which evident rings and gaps are seen in dust emission, and they are found to lie close to peaks in the disk gas density (Yen et al. 2019a). We also attempted to determine the magnetic lever arm  $\lambda$  in the wind by comparing the observed trends of the wind parameters along the shells with the predictions of models of magnetized winds from either a laminar AD-dominated or a fully turbulent disk. The characteristics of the HL Tau wind turn out to be intermediate between the two types of solutions, with a value of  $\lambda \sim 4 - 5$ . We discuss this finding in comparison to the input parameters of the models. The retrieved launching region between 50 and 90 au would point to a wind from an AD-dominated outer disk, but solutions with such a high value of  $\lambda$  do not exist and have yet to be found (current solutions reach  $\lambda = 2.76$ ). A possibility would be to consider solutions for a higher level of AD than is usually assumed, which may be applicable if the wind itself screens the incoming ionizing cosmic rays by magnetic mirroring (Cleeves et al. 2015). An increased field amplitude in the outer disk region with respect to the one commonly adopted could also help justify the high value of  $\lambda$ , as the ejection efficiency in the wind would be higher.

A magnetically driven disk wind with the above characteristics could sustain disk accretion at large scale by removing angular momentum in regions where the effective turbulence is suppressed because of weak internal ionization. This may have profound implications for the evolution of the disk and the formation of planets. In addition, the presence of distinct nested wind shells rooted in outer rings of enhanced gas density appears to support the results of recent non-ideal MHD numerical simulations for AD-dominated disks, which see the spontaneous formation of a ring-gap substructure in the disk connected with an inhomogeneous layered flow (e.g. Suriano et al. 2019; Riols et al. 2020), in a way alternative to the action of the yet elusive protoplanets.

The inferred properties of the CO wind call for further analyses of both observational and theoretical type. An analogous scrutiny of the fainter components and substructures in both the red- and blue-shifted lobes in the same datacube, as well as the challenging estimate of the mass and angular momentum transported in each shell, requires the development of dedicated procedures, which is currently underway (Nony et al., *in prep.*). On the theoretical side, it would be interesting to consider the extension of the numerical simulations of inhomogeneous layered disk winds to the large scales probed by our observations. Then, a comparison of the retrieved results with other classes of wind models is to be attempted, and it will be the subject of future works. Finally, new observational campaigns for this and other systems, currently in progress, will allow us to analyze the dynamic relationship between the outer CO outflow, the coaxial H<sub>2</sub> wind and the atomic jet.

These investigations are expected to provide further insight on the nature of the ejection phenomenon and finally to make us able to quantify the feedback of the winds on the disk evolution.

**Acknowledgements.** This paper uses ALMA data 2018.1.01037.S (PI L. Podio). ALMA is a partnership of ESO (representing its member states), NSF (USA) and NINS (Japan), together with NRC (Canada), MOST and ASIAA (Taiwan), and KASI (Republic of Korea), in cooperation with the Republic of Chile. The authors are grateful to G. Lesur for fruitful discussions and the support in the use of the self-similar MHD wind solutions he made publicly available at: <https://github.com/glesur/PPDwind>. The authors thank Z.-Y. Li, Y. Bai, T. Downes, F. Louvet, D. Fedele and L. Testi for fruitful discussions, and K. Rylg for help on data treatment. This work was supported by Large Grant INAF

2022 'YSOs Outflows, Disks, and Accretion: towards a global framework for the evolution of planet-forming systems (YODA)'. Part of the research activities were carried out with the contribution of the Next Generation EU funds within the National Recovery and Resilience Plan (PNRR), Mission 4 - Education and Research, Component 2 - From Research to Business (M4C2), Investment Line 3.1 - Strengthening and creation of Research Infrastructures, Project IR0000034 - "STILES - Strengthening the Italian Leadership in ELT and SKA". LP and CC acknowledge the projects PRIN-MUR 2020 - "BEYOND-2p: Astrochemistry beyond the second period elements" (Prot. 2020AFB3FX); ASI-Astrobiologia 2023 - "MIGLIORA-Modeling Chemical Complexity", (F83C23000800005); INAF-GO 2023 - "PROTO-SKA-Exploiting ALMA data to study planet-forming disks: preparing the advent of SKA" (C13C23000770005); INAF MiniGrant 2022 - "Chemical Origins" (PI: L. Podio); National Recovery and Resilience Plan (PNRR), Mission 4, Component 2, Investment 1.1, Call for tender No. 104 - Next Generation EU - 2022J2Y93 "Chemical Origins: linking the fossil composition of the Solar System with the chemistry of protoplanetary disks" (CUP J53D23001600006) - Grant Assignment Decree No. 962 adopted on 30.06.2023 by the Italian Ministry of University and Research.

## References

- Ai, T.-H., Liu, C.-F., Shang, H., Johnstone, D., & Krasnopolsky, R. 2024, *ApJ*, 964, 147
- Alexander, R., Pascucci, I., Andrews, S., Armitage, P., & Cieza, L. 2014, in *Protostars and Planets VI*, ed. H. Beuther, R. S. Klessen, C. P. Dullemond, & T. Henning, 475–496
- ALMA Partnership, Brogan, C. L., Pérez, L. M., et al. 2015, *ApJ*, 808, L3
- Anderson, J. M., Li, Z.-Y., Krasnopolsky, R., & Blandford, R. D. 2003, *ApJ*, 590, L107
- Andrews, S. M., Huang, J., Pérez, L. M., et al. 2018, *ApJ*, 869, L41
- Anglada, G., López, R., Estalella, R., et al. 2007, *AJ*, 133, 2799
- Bacciotti, F., Ray, T. P., Mundt, R., Eisloffel, J., & Solf, J. 2002, *ApJ*, 576, 222
- Beck, T. L., McGregor, P. J., Takami, M., & Pyo, T.-S. 2008, *ApJ*, 676, 472
- Béthune, W., Lesur, G., & Ferreira, J. 2017, *A&A*, 600, A75
- Bjerkeli, P., van der Wiel, M. H. D., Harsono, D., Ramsey, J. P., & Jørgensen, J. K. 2016, *Nature*, 540, 406
- Blandford, R. D. & Payne, D. G. 1982, *MNRAS*, 199, 883
- Casse, F. & Ferreira, J. 2000a, *A&A*, 353, 1115
- Casse, F. & Ferreira, J. 2000b, *A&A*, 361, 1178
- Cleeves, L. I., Bergin, E. A., Qi, C., Adams, F. C., & Öberg, K. I. 2015, *ApJ*, 799, 204
- Codella, C., Podio, L., Garufi, A., et al. 2020, *A&A*, 644, A120
- Cui, C. & Bai, X.-N. 2021, *MNRAS*, 507, 1106
- De Valon, A. 2021, PhD thesis, Université de Grenoble Alpes
- de Valon, A., Dougados, C., Cabrit, S., et al. 2020, *A&A*, 634, L12
- de Valon, A., Dougados, C., Cabrit, S., et al. 2022, *A&A*, 668, A78
- Delabrosse, V., Dougados, C., Cabrit, S., et al. 2024, *arXiv e-prints*, arXiv:2403.19400
- Fernández-López, M., Zapata, L. A., Rodríguez, L. F., et al. 2020, *AJ*, 159, 171
- Ferreira, J. 1997, *A&A*, 319, 340
- Ferreira, J., Dougados, C., & Cabrit, S. 2006, *A&A*, 453, 785
- Flock, M., Turner, N. J., Mulders, G. D., et al. 2019, *A&A*, 630, A147
- Frank, A., Ray, T. P., Cabrit, S., et al. 2014, in *Protostars and Planets VI*, ed. H. Beuther, R. S. Klessen, C. P. Dullemond, & T. Henning, 451–474
- Galli, P. A. B., Loinard, L., Ortiz-Léon, G. N., et al. 2018, *ApJ*, 859, 33
- Garufi, A., Podio, L., Codella, C., et al. 2021, *A&A*, 645, A145
- Garufi, A., Podio, L., Codella, C., et al. 2020, *A&A*, 636, A65
- Garufi, A., Podio, L., Codella, C., et al. 2022, *A&A*, 658, A104
- Hu, X., Li, Z.-Y., Zhu, Z., & Yang, C.-C. 2022, *MNRAS*, 516, 2006
- Jacquemin-Ide, J., Ferreira, J., & Lesur, G. 2019, *MNRAS*, 490, 3112
- Keppler, M., Benisty, M., Müller, A., et al. 2018, *A&A*, 617, A44
- Klaassen, P. D., Mottram, J. C., Maud, L. T., & Juhasz, A. 2016, *MNRAS*, 460, 627
- Lee, C.-F., Ho, P. T. P., Li, Z.-Y., et al. 2017, *Nature Astronomy*, 1, 0152
- Lee, C.-F., Li, Z.-Y., Codella, C., et al. 2018, *ApJ*, 856, 14
- Lee, C.-F., Mundy, L. G., Reipurth, B., Ostriker, E. C., & Stone, J. M. 2000, *ApJ*, 542, 925
- Lesur, G., Flock, M., Ercolano, B., et al. 2023, in *Astronomical Society of the Pacific Conference Series*, Vol. 534, *Protostars and Planets VII*, ed. S. Inutsuka, Y. Aikawa, T. Muto, K. Tomida, & M. Tamura, 465
- Lesur, G. R. J. 2021, *A&A*, 650, A35
- Lodato, G., Dipierro, G., Ragusa, E., et al. 2019, *MNRAS*, 486, 453
- López-Vázquez, J. A., Lee, C.-F., Fernández-López, M., et al. 2024, *ApJ*, 962, 28
- Louvet, F., Dougados, C., Cabrit, S., et al. 2018, *A&A*, 618, A120
- Lumbreras, A. M. & Zapata, L. A. 2014, *AJ*, 147, 72
- Martel, É. & Lesur, G. 2022, *A&A*, 667, A17

- McMullin, J. P., Waters, B., Schiebel, D., Young, W., & Golap, K. 2007, in *Astronomical Society of the Pacific Conference Series*, Vol. 376, *Astronomical Data Analysis Software and Systems XVI*, ed. R. A. Shaw, F. Hill, & D. J. Bell, 127
- Movsessian, T. A., Magakian, T. Y., & Moiseev, A. V. 2012, *A&A*, 541, A16
- Müller, H. S. P., Thorwirth, S., Roth, D. A., & Winnewisser, G. 2001, *A&A*, 370, L49
- Mundt, R., Buehrke, T., Solf, J., Ray, T. P., & Raga, A. C. 1990, *A&A*, 232, 37
- Nazari, P., Tabone, B., Ahmadi, A., et al. 2024, arXiv e-prints, arXiv:2402.18631
- Nisini, B., Navarro, M. G., Giannini, T., et al. 2024, *ApJ*, 967, 168
- Omura, M., Tokuda, K., & Machida, M. N. 2024, *ApJ*, 963, 72
- Pascucci, I., Beck, T. L., Cabrit, S., et al. 2024, arXiv e-prints, arXiv:2410.18033
- Pascucci, I., Cabrit, S., Edwards, S., et al. 2023, in *Astronomical Society of the Pacific Conference Series*, Vol. 534, *Protostars and Planets VII*, ed. S. Inutsuka, Y. Aikawa, T. Muto, K. Tomida, & M. Tamura, 567
- Pinte, C., Dent, W. R. F., Ménard, F., et al. 2016, *ApJ*, 816, 25
- Pinto, C., Galli, D., & Bacciotti, F. 2008, *A&A*, 484, 1
- Podio, L., Bacciotti, F., Fedele, D., et al. 2019, *A&A*, 623, L6
- Podio, L., Eisloffel, J., Melnikov, S., Hodapp, K. W., & Bacciotti, F. 2011, *A&A*, 527, A13
- Podio, L., Garufi, A., Codella, C., et al. 2020a, *A&A*, 642, L7
- Podio, L., Garufi, A., Codella, C., et al. 2020b, *A&A*, 644, A119
- Podio, L., Tabone, B., Codella, C., et al. 2021, *A&A*, 648, A45
- Pyo, T.-S., Hayashi, M., Kobayashi, N., et al. 2006, *ApJ*, 649, 836
- Rabeanahary, M., Cabrit, S., Meliani, Z., & Pineau des Forêts, G. 2022, *A&A*, 664, A118
- Ray, T. P. & Ferreira, J. 2021, *New A Rev.*, 93, 101615
- Riols, A. & Lesur, G. 2019, *A&A*, 625, A108
- Riols, A., Lesur, G., & Menard, F. 2020, *A&A*, 639, A95
- Segura-Cox, D. M., Schmiedeke, A., Pineda, J. E., et al. 2020, *Nature*, 586, 228
- Shang, H., Krasnopolsky, R., Liu, C.-F., & Wang, L.-Y. 2020, *ApJ*, 905, 116
- Shang, H., Liu, C.-F., Krasnopolsky, R., & Wang, L.-Y. 2023, *ApJ*, 944, 230
- Sheehan, P. D. & Eisner, J. A. 2017, *ApJ*, 840, L12
- Sheehan, P. D. & Eisner, J. A. 2018, *ApJ*, 857, 18
- Stephens, I. W., Lin, Z.-Y. D., Fernández-López, M., et al. 2023, *Nature*, 623, 705
- Suriano, S. S., Li, Z.-Y., Krasnopolsky, R., & Shang, H. 2018, *MNRAS*, 477, 1239
- Suriano, S. S., Li, Z.-Y., Krasnopolsky, R., Suzuki, T. K., & Shang, H. 2019, *MNRAS*, 484, 107
- Tabone, B., Cabrit, S., Bianchi, E., et al. 2017, *A&A*, 607, L6
- Tabone, B., Cabrit, S., Pineau des Forêts, G., et al. 2020, *A&A*, 640, A82
- Tabone, B., Raga, A., Cabrit, S., & Pineau des Forêts, G. 2018, *A&A*, 614, A119
- Takami, M., Beck, T. L., Pyo, T.-S., McGregor, P., & Davis, C. 2007, *ApJ*, 670, L33
- Welch, W. J., Hartmann, L., Helfer, T., & Briceño, C. 2000, *ApJ*, 540, 362
- Yen, H.-W., Gu, P.-G., Hirano, N., et al. 2019a, *ApJ*, 880, 69
- Yen, H.-W., Takakuwa, S., Gu, P.-G., et al. 2019b, *A&A*, 623, A96
- Zapata, L. A., Lizano, S., Rodríguez, L. F., et al. 2015, *ApJ*, 798, 131
- Zhang, Y., Arce, H. G., Mardones, D., et al. 2016, *ApJ*, 832, 158
- Zhang, Y., Arce, H. G., Mardones, D., et al. 2019, *ApJ*, 883, 1
- Zimniak, N., Ferreira, J., & Jacquemin-Ide, J. 2024, *A&A*, 692, A99



## Appendix A: Atlas of velocity channel maps

Figures A.1 and A.2 present an atlas of channel maps of CO (2-1) emission at  $V_{\text{LSR}}$  from  $-3.0 \text{ km s}^{-1}$  to  $+28.6 \text{ km s}^{-1}$ , in steps of  $0.4 \text{ km s}^{-1}$ . The panels at  $V_{\text{LSR}}$  from  $+3.0$  to  $+8.6 \text{ km s}^{-1}$  are centered on the source, to visualize the low-velocity emission in both lobes, while outside this range, emission is detected only in either the blue- or the red-shifted lobe, so the maps cover the relevant quadrant, with the source positioned in one corner.

The emission in the blue-shifted NE lobe is very faint. It consists of a large arc-shaped feature opening toward the NE seen at progressively larger distances from the source with increasing blue-shifted velocities. A fingerlike feature is identified at almost all velocities in about the same position north to the source and appears to be independent of the moving arc.

The red-shifted SW lobe is distributed in two main components, a wide-angle low-velocity wind and an inner faster flow of apparent conical shape with inscribed a series of arcs and bubble-like features. Each of these features can be followed over a number of adjacent channels, and it maintains the same shape and orientation with respect to the axis. The distance from the source and the size of each feature increase monotonically with  $V_{\text{LSR}}$ . As an example, Fig. A.3 illustrates the shift in position of the arc-shaped structures of family B (cf. Table 1) with increasing velocity.

The base of the red-shifted wind (with reference to the SE side with respect to the axis, as the NW side hosts the emission from the receding part of the disk) appears resolved in the channel maps at low velocities between  $V_{\text{LSR}} = 7.4$  and  $9.4 \text{ km s}^{-1}$ . Although the emission pattern is not clear, this velocity interval is consistent with the one expected under the DW hypothesis. In this scenario, the flow starts with  $V_p = 0$  at the footpoint (corresponding to  $V_{\text{LSR}} = V_{\text{sys}}$ ), and it is gradually faster as it leaves the disk. However, due to the absorption of the ambient medium, no material with  $V_{\text{LSR}} \leq 7.3 \text{ km s}^{-1}$  is visible (see, e.g. Fig. 4). On the other hand, the maximum  $V_{\text{LSR}}$  at which the wind base will be imaged is  $V_{\text{LSR}} = V_{\text{sys}} + V_p^* \cos i$ , where  $V_p^*$  is the poloidal velocity achieved at an altitude  $h = s / \cos(i) \sim 60 \text{ au}$  above the disk. Compared with the curves of the DW model discussed in Section 5.4,  $V_p^*$  is expected to be between  $2.0$  and  $3.5 \text{ km s}^{-1}$  from B2 to B1a (see Fig. 10, where the observed quantities are normalized by the corresponding  $r_0$  and  $V_K(r_0)$ ). Projecting along the l.o.s. and adding  $V_{\text{sys}}$ , one finds that the base of the flow should be visible in channel maps up to  $V_{\text{LSR}} \sim 8.4 - 9.5 \text{ km s}^{-1}$ , as we find, with the highest  $V_{\text{LSR}}$  corresponding to inner B1a. As predicted by the models, in the channel maps at  $V_{\text{LSR}} > 9.5 \text{ km s}^{-1}$  the wind base is not resolved.

## Appendix B: Atlas of transverse Position-Velocity diagrams

Figure B.1 presents an atlas of the transverse Position-Velocity diagrams ( $PV_{\perp}$ ) obtained for the red lobe with a  $0''.3$ -wide virtual slit centered on the axis and oriented at  $PA=318^\circ$  (i.e. perpendicular to the axis and with positive offsets toward NW), at separations  $y$  from the source from  $3''.5$  to  $10''$  in steps of  $0''.5$ . See Section 3.5 for a detailed description.

## Appendix C: Influence of wiggling and precession

We tested the influence of wiggling and precession on the derivations in Section 4.1 by analyzing the deviation of the centers of the fitted ellipses of the B features with respect to the axis  $x = 0$

of the  $PV_{\perp}$  diagrams (the perpendicular to the virtual slit of the diagram), corresponding in the sky to  $PA = 228^\circ$ . It can be shown that the axis of propagation of the shells deviates slightly from this direction, by  $0.5$ ,  $2$  and  $3$  degrees toward SE, for the B1a, B1b and B2 shells, respectively. The scatter of the centers with respect to these axes shows a hint of wiggling pattern consistent among the shells, but the shift is anywhere lower than  $3/5$  of the observational uncertainty on the shell radius. In any case, our derivation of  $r$ ,  $V_z$  and  $V_{\phi}$  relies on the relative positions of the apexes of the ellipses at the borders of the flow and does not use the information on the position of the ellipse center. Therefore, the determination of these quantities is not affected by wiggling, as long as the shell retains its coherence. In contrast, the different PA of the flow with respect to the perpendicular to the virtual slit can introduce a bias. We checked the importance of this effect by evaluating the expected variation in the worst case, that is for shell B2 at a large offset  $y = 9''.5$  from the star. The difference between the measured and real values of  $r$  and  $z$  is negligible, while the measured  $V_z$  turns out to be larger by  $1\%$  of the real one, and  $V_{\phi}$  smaller by  $8\%$ . In any case, these values are lower than the observational uncertainty of  $10\%$  on the velocities, which justifies the adoption of Eq. (1) for our analysis.

## Appendix D: Estimate of the radial velocity $V_r$

In Section 4.1 the assumption has been made that the wind streams along the detected shells. Formally, this translates into the fact that in the cylindrical coordinate system aligned with the red-shifted flow axis  $z$  and centered on the star, the poloidal velocity  $V_p = V_r \hat{e}_r + V_z \hat{e}_z$  is tangent to the shell surface. To test the validity of this assumption, one should verify that  $V_r/V_z = \tan(\alpha)$ , where  $\alpha$  is the local tangent angle to the shell, determined from the derivative of the measured  $r = r(z)$  and reported in Table 1. While  $V_z$  and  $\alpha$  are found from the measurements at the lateral apexes of the fitted ellipses, the search for  $V_r$  is complicated by the combination of the detected variation of  $V_z$  along the shell and the inclination of the flow axis. With reference to Fig. D.1, and assuming axisymmetry, to determine the radial velocity  $V_r$  corresponding to the axial velocity  $V_z$  evaluated at offset  $Y_0$ , one has to measure the  $V_{\text{LSR}}$  at either point A or B of the same shell section (the blue circle in the figure), that is at the points where the projection of  $V_{\phi}$  along the l.o.s. vanishes:

$$V_r = \frac{V_{\text{LSR}}(B) - V_z \cos i - V_{\text{sys}}}{\sin i} = \frac{V_z \cos i + V_{\text{sys}} - V_{\text{LSR}}(A)}{\sin i}. \quad (\text{D.1})$$

However, points A and B fall at offsets  $Y_0 \pm R_0(Y_0) \cos i$ . Unfortunately, with the given geometry, these points correspond in almost all cases to regions of the diagrams with faint or confused emission, out of the field of view, hidden by the brightness of the gas close to the source or lost because of the CO autoabsorption around  $V_{\text{sys}}$ . These factors make the determination of  $V_r$  extremely difficult.

In practice, this quantity could be reasonably determined only for shell B2 in the two positions at  $9''.5$  and  $10''$ , using the cleaner diagram  $PV_{\parallel}$ , and limiting the search to the upper point of type B. Taking into account the radius of the shell in these positions, the searched point B is found at offsets  $4''.9$  and  $5''.3$ , where one finds  $V_{\text{LSR}}(B) = 14.8 \pm 0.3 \text{ km s}^{-1}$  and  $15.7 \pm 0.3 \text{ km s}^{-1}$ , respectively. Equation D.1 then leads to  $V_r = 2.1 \pm 0.4 \text{ km s}^{-1}$  and  $2.9 \pm 0.4 \text{ km s}^{-1}$ . In turn, the orientation angle of  $V_p$

with respect to the  $z$  axis turns out to be  $12.9^\circ \pm 3.0^\circ$  at offset  $9''.5$  and  $16.9^\circ \pm 3.2^\circ$  at offset  $10''$ . According to Table 1, the tangent angle  $\alpha$  at these positions is  $15.5^\circ$  and  $14.9^\circ$ , which implies that here  $V_p$  is compatible with being tangential to the shell surface within the errors.

### Appendix E: Comparison with models - variation of $\lambda_\phi$ along the streamline

Figure E.1 illustrates the similarity of the trend of variation of the specific angular momentum  $\lambda_\phi$  along a streamline. Models L2 (Lesur 2021) and N5 (Zimniak et al. 2024) are calculated for  $r_0=1$  au and a star of solar mass. The points for shell B2 are normalized by the retrieved footpoint radius and corresponding Keplerian velocity for a stellar mass of  $2.1 M_\odot$ . In this way the wind streamline originates in all cases at 1 au, where it is usual to assume that the turbulence starts, so as to have the most effective comparison between the turbulence- and AD-dominated disk wind models (N and L types of solutions, respectively). In all cases the values are seen to follow closely the curve at constant  $r_0=1$ , with a progression toward higher  $\lambda_\phi$  with distance, as expected in steady MHD disk winds.

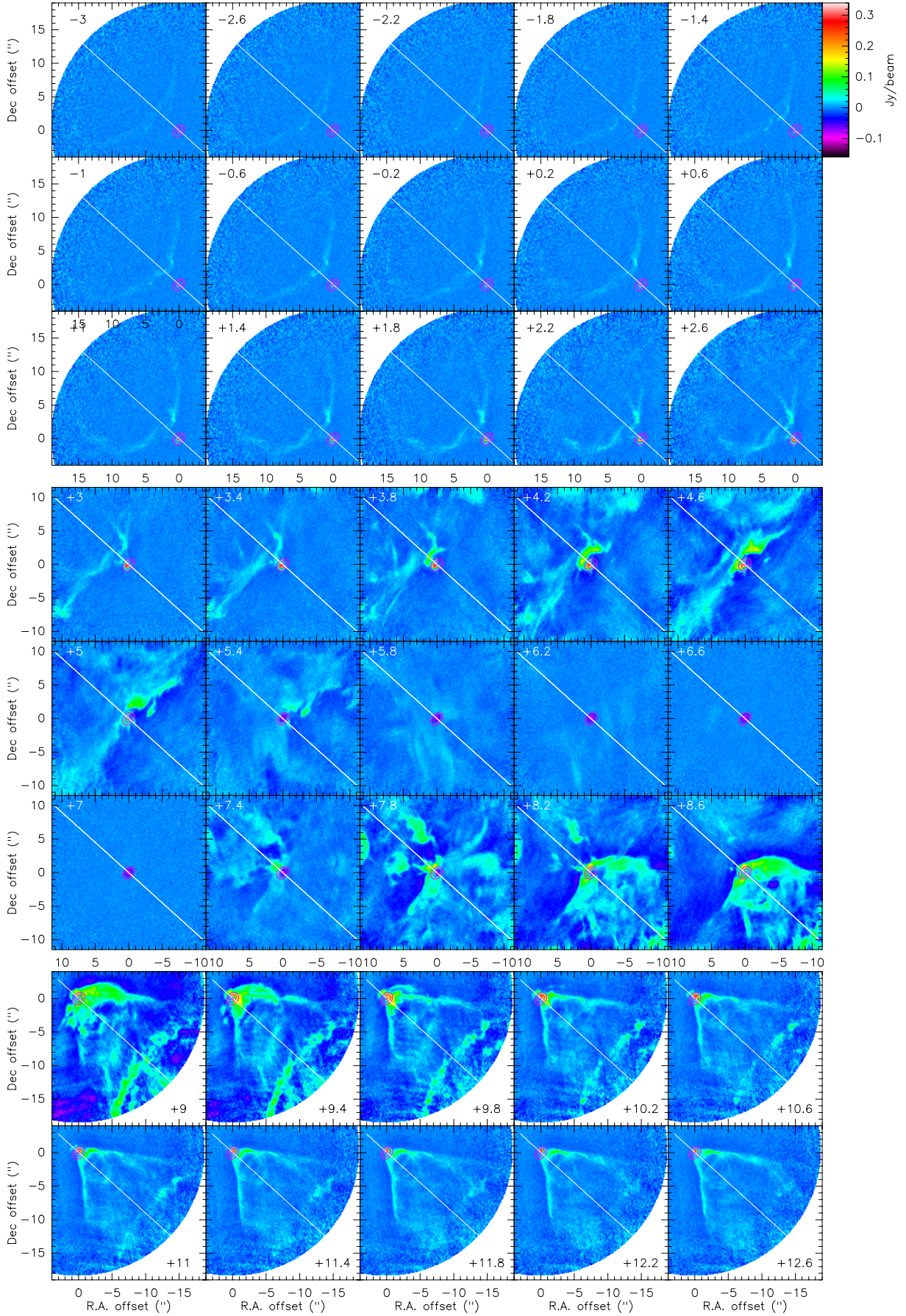


**Fig. A.1.** Channel maps of the CO (2-1) emission with  $V_{\text{LSR}}$  velocity from  $-3$  to  $+12.6$   $\text{km s}^{-1}$ . The beam size is  $0''.31 \times 0''.26$  ( $\text{PA} = -3^\circ$ ), corresponding to a spatial resolution of about 40 au at the distance of HL Tau (147.3 pc). In all the panels the disk position is indicated by the magenta contours of the continuum emission at 1.3mm, drawn at  $[10, 200, 700]\sigma_c$ . The white line indicates the direction of the disk minor axis ( $\text{PA} = 48^\circ$ ).

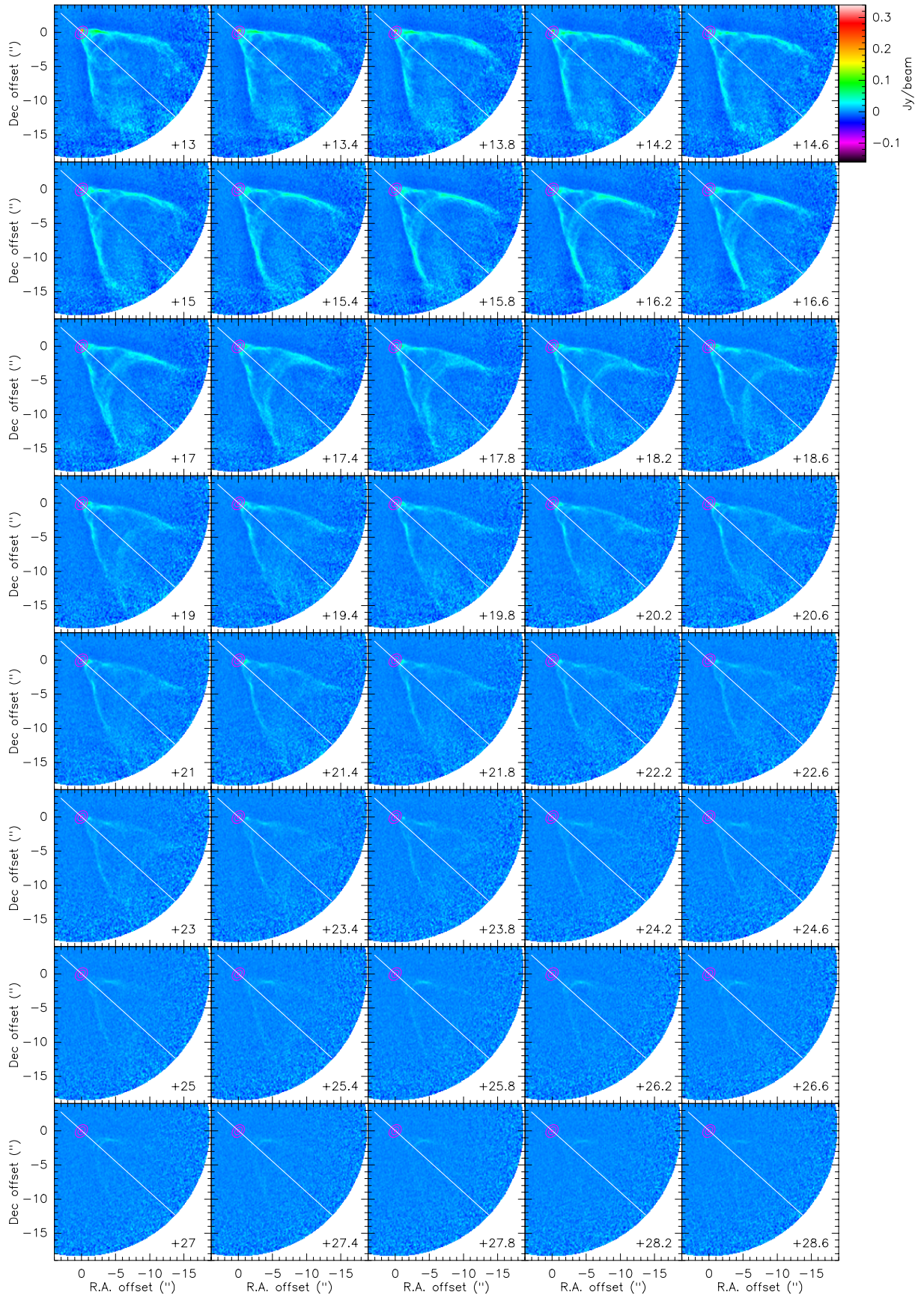


**Fig. A.2.** Same of Fig.A.1, for the channel maps with  $V_{\text{LSR}}$  from +13 to +28.6  $\text{km s}^{-1}$ .

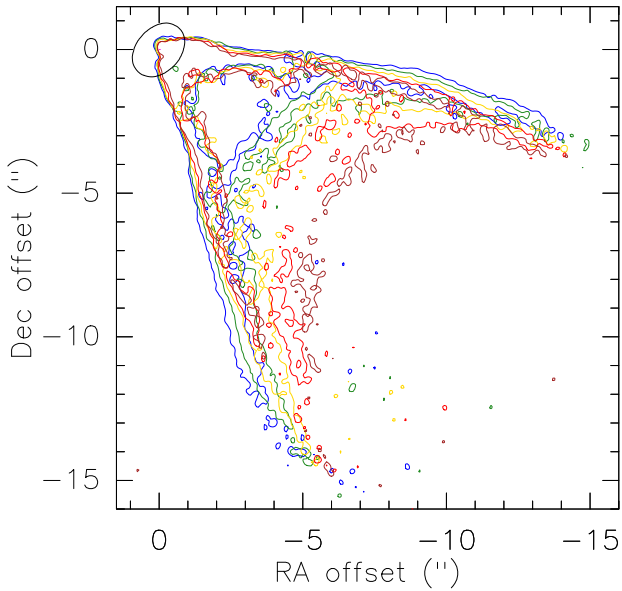


**Fig. A.3.** Contours of the CO emission at  $4\sigma_{\text{CO}}$  in the channels at 15.4 (blue), 16.2 (green), 17.0 (yellow), 17.8 (red) and 18.6 (brown)  $\text{km s}^{-1}$ . The disk is indicated by a black contour at  $10\sigma_c$ . The structures are seen at progressively larger separations from the source in contiguous channel maps.

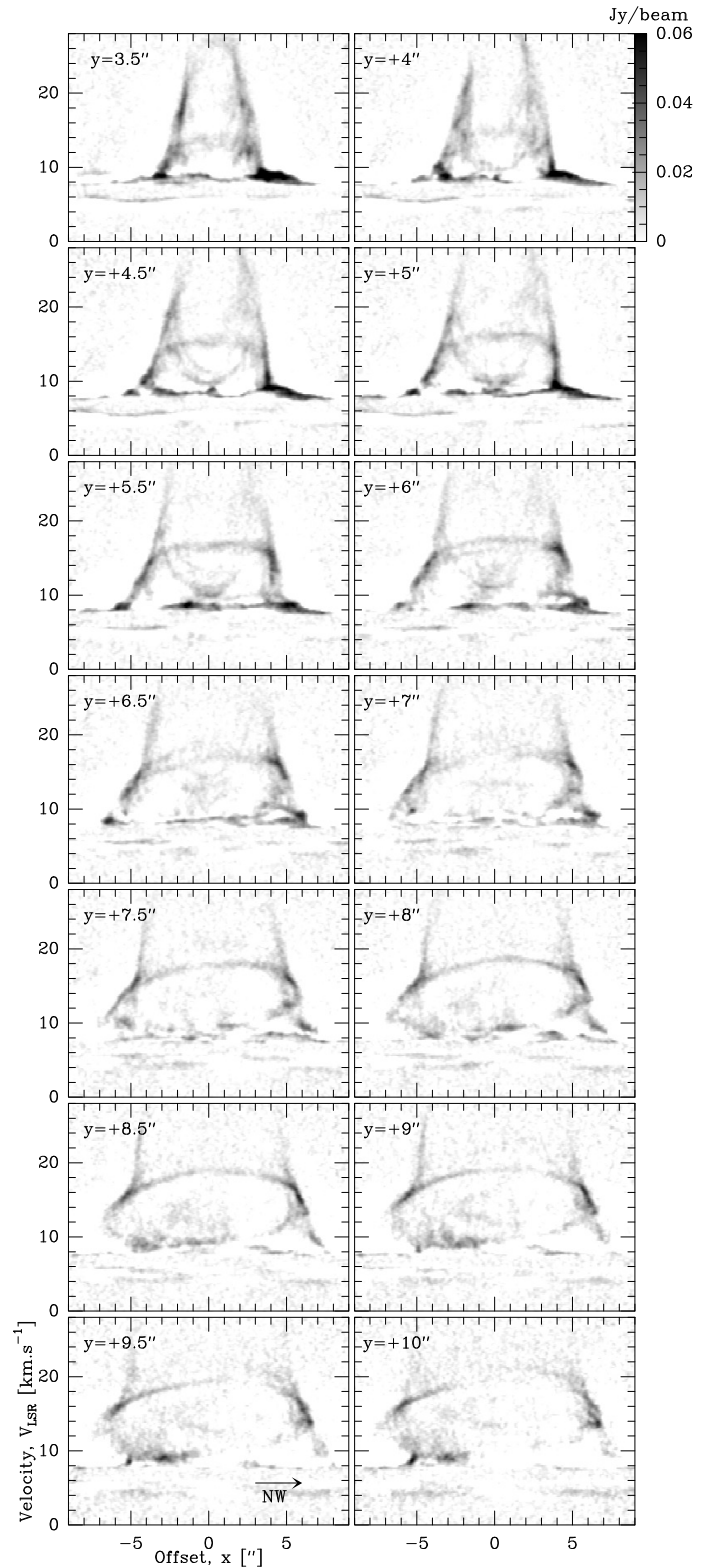


**Fig. B.1.** Position-Velocity diagrams taken across the red-shifted outflow lobe ( $PV_{\perp}$  diagrams), with the virtual slit centered on the flow axis and perpendicular to it ( $PA = 318^{\circ}$ ), with positive  $x$  offsets toward NW. The separation of the virtual slit from the source in arcseconds is given in the upper-left corner.

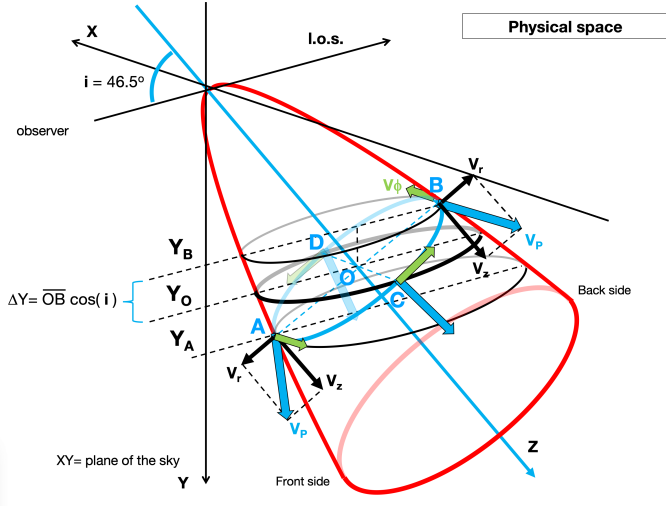


**Fig. D.1.** Sketch showing the geometry of the flow in physical space relative to the determination of the radial component of the velocity  $V_r$ , in the general case in which the poloidal velocity  $V_p$  does not lie along the shell surface (see text).

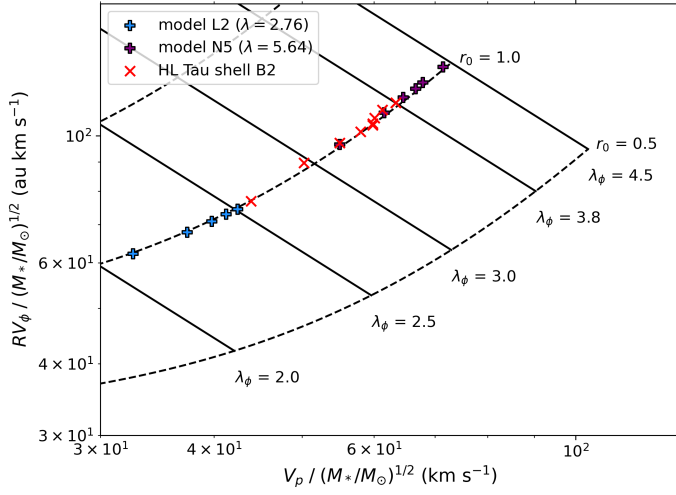


**Fig. E.1.** Trend of the specific angular momentum  $\lambda_\phi$  along a streamline originating from 1 au in a disk around a  $1 M_\odot$  star following models L2 (blue) and N5 (purple), for separations from the source  $z/r_0 = 10, 20, 30, 40, 50$  from left to right, with an additional point at  $z/r_0 = 100$  for model N5. Superposed red crosses illustrate the trend for  $\lambda_\phi$  along shell B2 as in Table 1, after normalization of  $r$ ,  $V_p$  and  $V_\phi$  by the derived footpoint radius  $r_0 = 86$  au and corresponding Keplerian velocity at  $r_0$ , for  $M_* = 2.1 M_\odot$  (see Section 5.4).